

Adaptive concurrent multi-level model for multi-scale analysis of ductile fracture in heterogeneous aluminum alloys



Somnath Ghosh ^{a,*}, Daniel Paquet ^b

^a Department of Civil Engineering, Johns Hopkins University, 203 Latrobe, 3400 N. Charles Street, Baltimore, MD 21218, United States

^b Department of Mechanical Engineering, The Ohio State University, Scott Laboratory, Columbus, OH 43210, United States

ARTICLE INFO

Article history:

Received 1 November 2012

Received in revised form 22 April 2013

Available online 1 June 2013

Keywords:

Ductile fracture

Heterogeneous aluminum alloys

Adaptive multi-scale model

LE-VCFEM

Homogenization based plasticity-damage (HCPD) model

ABSTRACT

This paper creates a novel adaptive multi-level modeling framework for rate-dependent ductile fracture of heterogeneous aluminum alloys with non-uniform microstructures. The microstructure of aluminum alloys is characterized by a dispersion of brittle heterogeneities such as silicon and intermetallics in a ductile aluminum matrix. These microstructural heterogeneities affect their failure properties like ductility in an adverse manner. The multi-level model invokes two-way coupling, viz. homogenization for upscaled constitutive modeling, and top-down scale-transition in regions of localization and damage. Adaptivity is necessary for incorporating continuous changes in the computational model as a consequence of evolving microstructural deformation and damage. The macroscopic finite element analysis in regions of homogeneity incorporates homogenization-based continuum rate-dependent plasticity-damage (HCPD) models. Transcending scales is required in regions of high macroscopic gradients caused by underlying localized plasticity and damage. Complete microscopic analysis using the LE-VCFEM is conducted in these regions, which follow the growth of microscopic voids and cracking to cause local ductile fracture. The macroscopic and microscopic simulations are done concurrently in a coupled manner. Physics-based level change criteria are developed to improve the accuracy and efficiency of the model. Numerical simulations are conducted for validations and ductile fracture in a real microstructure is demonstrated.

© 2013 Elsevier Ltd. All rights reserved.

1. Introduction

Heterogeneous cast aluminum alloys, containing silicon and intermetallic inclusions in the dendritic structure, are widely used in automotive and aerospace structures. While higher strength may result from the presence of these heterogeneities in the microstructure, failure properties like ductility are generally adversely affected. Major microstructural mechanisms responsible for deteriorating these properties include particulate fragmentation and matrix cracking. Ductile failure generally initiates with second phase inclusion fragmentation. Large plastic

strains in the vicinity of damaged inclusions lead to void nucleation in the matrix. Damage subsequently propagates with void growth and localizes in bands of intense plastic deformation between inclusions, until void coalescence in the matrix leads to catastrophic failure. Experimental studies e.g. in Caceres et al. (1996), Caceres (1999), Wang et al. (2003) have shown strong connections between morphological variations and microstructural damage nucleation and growth. The studies have shown that damage initiation is mainly controlled by the shape of inclusions in the microstructure, while the rate of damage evolution at higher strains is controlled by the level of clustering. This makes predicting ductility quite challenging.

* Corresponding author. Tel.: +1 410 516 7833; fax: +1 410 516 7473.
E-mail address: sghosh20@jhu.edu (S. Ghosh).

Computational studies have been conducted to study elastic–plastic deformation and ductile failure of heterogeneous materials in Steglich and Brocks (1997), Lim and Dunne (1996), Negre et al. (2003), Huber et al. (2005), Llorca and Gonzalez (1998), Llorca and Segurado (2004). The predictive capability of some of these unit cell models for failure properties is limited due to over-simplification of the microstructure. Quite often, critical local features necessary to model strain to failure are lost in these models. Ductile fracture depends strongly on the extreme values of microstructural characteristics, e.g. nearest neighbor distances, highest local volume fraction etc. and computational models must feature some of these characteristics for accuracy. Additionally, many studies have focused only on the initial stages of ductile damage, e.g. crack nucleation and have not considered their evolution to failure. There is a paucity of image-based models that consider aspects of the real microstructural morphology and non-uniformities. Computational models developed by Ghosh et al. (Moorthy and Ghosh, 1998, Ghosh and Moorthy, 1998, Hu and Ghosh, 2008, Paquet et al., 2011a,b) have focused on realistic representation of microstructures with non-uniform dispersion of heterogeneities. The microstructural Voronoi cell finite element model (VCFEM) developed in Moorthy and Ghosh (2000), Ghosh (2011), Ghosh et al. (2000), Moorthy and Ghosh (1998), Ghosh and Moorthy (1998) is very accurate and efficient for micromechanical analysis. Morphological non-uniformities in dispersions, shapes and sizes of micrographs are readily modeled by this method. The method has been extended in the locally enhanced VCFEM (LE-VCFEM) to model stages of ductile fracture in Hu and Ghosh (2008), from inclusion fragmentation to matrix cracking in the form of void nucleation, growth and coalescence. In LE-VCFEM (Hu and Ghosh, 2008), the stress-based hybrid VCFEM formulation is adaptively altered. Regions of localized plastic flow are overlaid with finite deformation, displacement-based elements to accommodate strain softening. LE-VCFEM has been demonstrated to be very effective for simulating ductile fracture for rate-independent and rate-dependent plasticity in Hu and Ghosh (2008), Paquet et al. (2011a,b), respectively.

Pure micromechanical analysis of an entire structure is however computationally prohibitive due to the large number of heterogeneities in the underlying microstructure. The need for multi-scale modeling, with micromechanisms of damage explicitly modeled only in regions of localization and cracking, is realized for these problems. Different classes of multi-scale models have been developed in the literature.

- Classical, first-order homogenization methods have been developed e.g. in Guedes and Kikuchi (1990), Ghosh et al. (1995), Feyel and Chaboche (2000), Terada and Kikuchi (2001), Miehe and Koch (2002), Ghosh et al. (1996), Lee and Ghosh (1996), Moulinec and Suquet (2001), Zohdi et al. (1999), Oden and Zohdi (1997) based on the asymptotic expansion theory of homogenization (Benssousan et al., 1978; Sanchez-Palencia et al., 1983). This theory assumes a complete separation of scales and does not incorporate length-scale effects.

These homogenization methods capture relatively uniform macroscopic deformation fields without large gradients in the deformation fields or localized softening behavior.

- Higher-order homogenization methods have been developed e.g. in Kouznetsova et al. (2004), Luscher et al. (2010), Vernerey et al. (2008), Fish and Kuznetsov (2010), Loehnert and Belytschko (2007) for transferring higher-order kinematics from the micro-scale to macro-scale. This results in the introduction of a length-scale parameter in the model, e.g. the size of the RVE. The limited number of higher-order kinematic variables however restricts their applicability in the event of high localization of deformation and damage.
- *Continuous-discontinuous* multi-scale models have been developed in Massart et al. (2007), Belytschko et al. (2008), Song (2009) to capture the local softening arising in the microscopic scale due to damage. These methods are based on the partitioning of the RVE into sub-domains delineating regions in which the material response is stable and unstable. Classical homogenization method is used for the overall behavior of the stable sub-domain. The homogenization method for the unstable sub-domain is specific to the type of damage considered. The behavior and geometry of material instabilities in the RVE need to be well defined. The accuracy of the method strongly depends on the assumptions made for the description of the equivalent discontinuities at the macro-scale.
- *Multi-level*, multi-scale models e.g. in Vemaganti and Oden (2001), Markovic and Ibrahimbegovic (2004), Temizer and Wriggers (2011), Kim et al. (2010), Miehe and Bayreuther (2007), Fish and Shek (2000), Zohdi and Wriggers (1999) require that complete micromechanical analyses be performed in portions of the computational domain that are undergoing intense deformation and damage. The effects of microstructural instabilities are fully captured with the micromechanical model. Classical homogenization method is used for upscaling the mechanical behavior in the macroscopic sub-domains, for which there is no localization of deformation and damage. The effect of microstructural damage in the microscopic sub-domains is transferred to the macroscopic sub-domains by coupling the two scales of analysis.

Ghosh and co-workers have developed adaptive multi-level, multi-scale models for: (i) linear elastic composites (Raghavan et al., 2001, Raghavan and Ghosh, 2004, Raghavan and Ghosh, 2004), (ii) elastic–plastic composite materials undergoing microstructural damage by inclusion cracking only (Lee et al., 1999; Ghosh, 2011), and (iii) composites with interfacial debonding in Raghavan et al. (2004), Ghosh et al. (2007). Developments of the multi-scale analysis using VCFEM micromechanical analyses have been discussed in Ghosh (2011). These multi-scale models involve two-way coupling, viz. homogenization for upscaled constitutive modeling, and top-down scale-transition in regions of localization and damage. Multi-scale characterization and domain partitioning have also been developed as a pre-processor to multi-scale modeling

in Valiveti and Ghosh (2007), Ghosh et al. (2006) for determining microstructural representative volume elements, as well as for identifying regions where homogenization breaks down.

The present paper, assimilates a variety of complementary ingredients from the previous developments to create a novel multi-level modeling framework for ductile fracture. The adaptive multi-level computational model is developed for rate-dependent ductile fracture in heterogeneous aluminum alloys with non-uniform microstructures. This extension incorporates complex mechanisms of damage nucleation by particle cracking, subsequent void growth in the matrix and coalescence. Adaptivity is necessary for incorporating continuous changes in the computational model as a consequence of evolving microstructural deformation and damage. The macroscopic finite element analysis in regions of low gradients and homogeneity incorporates homogenization-based continuum rate-dependent plasticity-damage (HCPD) models. Transcending scales is required in regions of high macroscopic gradients caused by underlying localized plasticity and damage. Complete microscopic analysis using the LE-VCFEM is conducted in these regions, which follow the growth of microscopic voids and cracking to cause local ductile fracture. The macroscopic and microscopic simulations are done concurrently in a coupled manner. The theory in this multi-scale formulation is a combination of small-strain and large-strain formulation in different regions of the domain. Small strain analysis formulation is applicable to the macroscopic plastic deformation regions that do not show much localization. A finite deformation formulation in a rotated Lagrangian system is developed for microstructural regions of localized deformation and ductile fracture that are modeled by the locally enhanced Voronoi cell elements or LE-VCFEM.

Appropriate level change criteria are developed to improve the accuracy and efficiency of the model. The overall multi-level model for multi-scale analysis of ductile fracture is presented in Section 2. Adaptivity criteria for evolution of the multi-level model are defined in Section 3, while coupling of the different levels are detailed in Section 4. Numerical simulations for validations are conducted in Section 5 and a real microstructure is demonstrated in Section 6.

2. Levels in the concurrent multi-scale modeling framework

The multi-level framework for multi-scale analysis adaptively decomposes the heterogeneous computational domain Ω_{het} into a set of non-intersecting sub-domains, denoted by *level-0*, *level-1*, *level-2*, and *level-tr*, i.e. $\Omega_{het} = \Omega_{l0} \cup \Omega_{l1} \cup \Omega_{l2} \cup \Omega_{tr}$. Concurrent multi-scale analysis requires that all levels be coupled for simultaneous solving of variables in the different sub-domains. The levels are defined as follows:

- (1) *Level-0*: In this subdomain Ω_{l0} , purely macroscopic computations are executed using continuum constitutive models that implicitly represent the effect of

the microstructure and its evolution. The constitutive material models are obtained by homogenizing the material response in the microstructural RVE as discussed in Section 2.1.3.

- (2) *Level-1*: This computational subdomain Ω_{l1} is used to establish criteria that necessitate switching over from macroscopic to microscopic computations. Details of this "swing" level are discussed in Section 2.2.
- (3) *Level-2*: This embedded computational subdomain Ω_{l2} requires pure microscopic analysis with delineation of the microstructure and its evolution.
- (4) *Transition interface layer*: This computational subdomain Ω_{tr} is sandwiched between the macroscopic (*level-0/level-1*) and microscopic (*level-2*) domains and acts as an interface region to regularize kinetic and kinematic incompatibilities.

Brief descriptions of each levels for ductile fracture are given next.

2.1. Computational subdomain level-0 (Ω_{l0})

The computational subdomain *level-0* (Ω^{l0}) invokes macroscopic finite element analysis using homogenized constitutive relations. It assumes uniform macroscopic deformation and periodic microstructural variables to admit homogenized response. Hierarchical models such as the FE² multi-scale methods (Feyel and Chaboche, 2000) solve the micromechanical RVE problem at every element integration point in the computational domain. This can lead to prohibitively large computational costs. To overcome this limitation, Ghosh et al. (2009) have developed macroscopic constitutive laws of elastic-plastic damage from homogenization of microscopic RVE response. Parameters in these constitutive models represent the effect of morphology, as well as evolving microstructural mechanisms. These reduced-order constitutive models are highly efficient as they do not have to account for the details of microstructural morphology or solve the micromechanical RVE problem in every step of an incremental process. This section summarizes a rate dependent homogenization-based continuum plasticity-damage (HCPD) model for macroscopic representation of ductile failure in porous viscoplastic materials containing brittle inclusions, that has been developed in Paquet et al. (2011), Dondeti et al. (2012).

- It is developed from homogenization of a microscopic RVE of a heterogeneous aluminum alloy with a non-uniform dispersion of inclusions, as shown in Fig. 1, following the Hill-Mandel postulate. Micromechanical analyses of the elastic-plastic RVE with inclusion and matrix cracking are conducted by LE-VCFEM (Hu and Ghosh, 2008; Paquet et al., 2011a).
- The anisotropic rate-dependent HCPD model in Paquet et al. (2011), Dondeti et al. (2012) has the framework of the Gurson-Tvergaard-Needleman model (Gurson, 1977; Chu and Needleman, 1980; Tvergaard, 1982; Tvergaard and Needleman, 1984). An anisotropic plastic

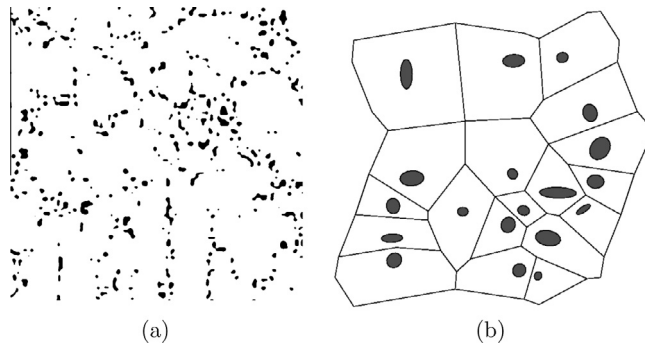


Fig. 1. (a) Micrograph of a cast aluminum alloy W319 ($192 \mu\text{m} \times 192 \mu\text{m}$) showing dendritic regions, (b) typical SERVE of the microstructure in (a) obtained for a characteristic size of $48 \mu\text{m}$ (Micrograph: Courtesy Ford Research Laboratory).

flow potential is introduced in an evolving material-damage principal coordinate system, in which parameters evolve as functions of the plastic work.

- A macroscopic void nucleation law is developed by homogenizing inclusion fragmentation results in the RVE. Rate effects and anisotropy are included in the nucleation law.

Important tasks in the development of the HCPD model includes: (i) identification of a statistically equivalent RVE or SERVE; (ii) detailed micromechanical analyses by LE-VCFEM including explicit mechanisms of plasticity and damage; (iii) homogenization with periodic boundary conditions for reduced-order modeling; (iv) framework development for rate-dependent anisotropic continuum plasticity and damage; and (v) calibration of the evolving model parameter functions.

2.1.1. Identification of the SERVE size for homogenization

The statistically equivalent representative volume element or SERVE is the smallest volume element of the microstructure exhibiting the characteristics: (i) effective constitutive material properties for the SERVE should equal those for the entire microstructure, and (ii) it should not depend on the location in the microstructure. Following methods of SERVE identification from actual micrographs of heterogeneous materials in Ghosh et al. (2009), Paquet et al. (2011), Dondeti et al. (2012), the present study uses the multivariate marked correlation function $M(r)$ to establish the SERVE. Marked correlation functions relate any geometric or response field variable with the microstructural morphology. In Ghosh et al. (2009), the marked correlation function $M(r)$ has been calculated with the micromechanical plastic work W_p as marks. A high value of $M(r)$ indicates a strong correlation between entities in the microstructure. $M(r)$ stabilizes to near-unity values at a characteristic radius of convergence r_0 , which signifies the limit of correlated variables. For $r \geq r_0$, $M(r) \approx 1$ and the local morphology ceases to have any significant influence on the field variables beyond this characteristic radial distance. The RVE size is estimated as $L_{RVE} \approx 2 \times r_0$, where r_0 corresponds to the local correlation length. For the cast aluminum alloy W319 microstructure in Fig. 1(b) the SERVE size has been established as $L_{RVE} = 48 \mu\text{m}$ in

Dondeti et al. (2012). This region corresponds to an intra-granular region containing secondary dendrite arms and inter-dendritic regions containing particulates. The nominal grain size of aluminum alloys is an order of magnitude larger than this SERVE (typically ~ 600 – $800 \mu\text{m}$). Mechanical properties in aluminum alloys have been shown to correlate better with the secondary dendritic arm spacing or SDAS rather than the grain size.

2.1.2. Micromechanical analyses by LE-VCFEM with mechanisms of plasticity and damage

The locally enhanced Voronoi cell finite element method or LE-VCFEM has been successfully developed in Hu and Ghosh (2008), Paquet et al. (2011a), Ghosh (2011) to model the evolution of microstructural failure from particle fragmentation to complete ductile failure by matrix cracking due to void growth and coalescence. In LE-VCFEM, the stress-based hybrid VCFEM formulation is enhanced adaptively in narrow bands of localized plastic flow and void growth. These regions are locally embedded with finite deformation, displacement-based elements to accommodate strain softening in the constitutive behavior. A summary of the constitutive and damage models for each phase in the microstructure of LE-VCFEM is given here.

The inclusion phase in each Voronoi cell element is assumed to be isotropic, linear elastic. Instantaneous cracking and fragmentation of the inclusion follows a Weibull distribution based initiation criterion, where a crack is introduced when the probability function P_{frag} at any point in the inclusion exceeds a critical value. The size-dependent probability function is expressed as:

$$P_{frag}(\nu, \sigma_I^c) = 1 - \exp \left[-\frac{\nu}{\nu_0} \left(\frac{\sigma_I^c}{\sigma_w} \right)^m \right] \quad (1)$$

m and σ_w are the Weibull modulus and characteristic strength respectively, ν_0 is a reference volume, ν is the inclusion size and σ_I^c is the maximum principal stress in the inclusion. The matrix phase is modeled as a rate-dependent elastic-viscoplastic porous material, extending the GTN model framework for rate dependent behavior in Paquet et al. (2011a). The total strain-rate in this model is assumed to admit an additive decomposition into an elastic and viscoplastic part, i.e. $\dot{\epsilon} = \dot{\epsilon}^e + \dot{\epsilon}^p$. For small strains, the rate of Cauchy stress is expressed as

$\dot{\sigma} = \mathbf{C}^e : \dot{\epsilon}^e$, where \mathbf{C}^e is the fourth order isotropic elasticity tensor. The viscoplastic behavior of the porous ductile matrix is governed by the GTN yield function as:

$$\phi^{vp} = \left(\frac{q}{\bar{\sigma}_M} \right)^2 + 2f^*q_1 \cosh \left(-\frac{3q_2 p}{2\bar{\sigma}_M} \right) - (1 + q_3 f^{*2}) = 0 \quad (2)$$

$q = \sqrt{\frac{3}{2}\boldsymbol{\sigma}' : \boldsymbol{\sigma}'}$ and $p = -\frac{1}{3}\boldsymbol{\sigma} : \mathbf{I}$ are the Von-Mises equivalent stress and the hydrostatic pressure respectively, $\boldsymbol{\sigma}'$ is the deviatoric stress and q_1, q_2, q_3 are void growth related parameters. f^* is a function of the void volume fraction f that is expressed in Eq. (9). The subscript M is used to designate association with the pure matrix material without voids and $\bar{\sigma}_M$ is the equivalent matrix stress. For the viscoplastic behavior (see Perzyna (1966)), an over-stress function F_M is defined as a measure of the excess stress over the rate-independent local yield strength σ_0 , and is expressed as:

$$F_M = \bar{\sigma}_M - \sigma_0(W_p) \quad (3)$$

The plastic strain-rate for the porous matrix is governed by the associated flow rule and is a function of the over-stress $\Phi_M(F_M)$, expressed as Paquet et al. (2011a):

$$\dot{\epsilon}^p = \lambda \frac{\partial \phi^{vp}}{\partial \boldsymbol{\sigma}} = (1-f) \sqrt{\frac{2}{3}} \frac{\bar{\sigma}_M}{\boldsymbol{\sigma} : \frac{\partial \phi^{vp}}{\partial \boldsymbol{\sigma}}} \gamma \Phi_M(F_M) \frac{\partial \Phi_M}{\partial \boldsymbol{\sigma}} \quad (4)$$

λ is a viscoplastic multiplier that is derived in terms of the matrix plastic strain-rate $\dot{\epsilon}_M^p$ using the Hill-Mandel energy equivalence and γ is a temperature dependent viscosity coefficient. A power law expression is chosen for $\Phi_M(F) = \langle F_M \rangle^p$ (Perzyna, 1966), where $\langle \cdot \rangle$ is the MacCauley operator. A linear hardening law governs the evolution of the yield strength σ_0 , expressed as:

$$\dot{\sigma}_0 = h(W_p) \dot{\epsilon}_M^p, \quad \text{where } \dot{\epsilon}_M^p = \sqrt{\frac{2}{3} \dot{\epsilon}_M^p : \dot{\epsilon}_M^p} = \sqrt{\frac{2}{3} \gamma \Phi_M(F_M)} \quad (5)$$

where $h(W_p)$ is the instantaneous plastic modulus. The rate of evolution of the local void volume fraction f is divided into growth and nucleation parts (Chu and Needleman, 1980; Tvergaard and Needleman, 1984) as:

$$\dot{f} = \dot{f}_{growth} + \dot{f}_{nucleation} \quad \text{where}$$

$$\dot{f}_{growth} = (1-f) \dot{\epsilon}_{kk}^p \quad \text{and}$$

$$\begin{aligned} \dot{f}_{nucleation} &= A(\dot{\epsilon}_M^p) \dot{\epsilon}_M^p, \quad A(\dot{\epsilon}_M^p) \\ &= \frac{f_N}{s_N \sqrt{2\pi}} \exp \left[-\frac{1}{2} \left(\frac{\dot{\epsilon}_M^p - \epsilon_N}{s_N} \right)^2 \right] \end{aligned} \quad (6)$$

Here ϵ_N is the mean nucleation strain, s_N is its standard deviation, and f_N is the intensity of void nucleation. To avoid mesh sensitivity in LE-VCFEM (Paquet et al., 2011a; Hu and Ghosh, 2008) a material length scale has been incorporated through a non-local model where the non-local growth rate of void volume fraction at a material point $\bar{\mathbf{x}}$ is given as:

$$\dot{f}_{non-local} = \frac{1}{W(\bar{\mathbf{x}})} \int_{\Omega_m} \dot{f}(\mathbf{x}) w(|\mathbf{x} - \bar{\mathbf{x}}|) d\Omega \quad (7)$$

where

$$W(\bar{\mathbf{x}}) = \int_{\Omega_m} w(|\mathbf{x} - \bar{\mathbf{x}}|) d\Omega \quad \text{and } w(|\mathbf{x}|) = \left[\frac{1}{1 + (|\mathbf{x}|/L)^p} \right]^q \quad (8)$$

Here $p = 8, q = 2$ and $L > 0$ is a material characteristic length. The weighting function $w(|\mathbf{x}|) = 1$ at $|\mathbf{x}| = 0$, $w(|\mathbf{x}|) = 0.25$ at $|\mathbf{x}| = L$ and $w(|\mathbf{x}|) \rightarrow 0 \forall |\mathbf{x}| > L$.

Finally, an acceleration function f^* is introduced in Eq. (2) to model the complete loss of material stress carrying capacity due to void coalescence (Tvergaard and Needleman, 1984) as:

$$f^* = \begin{cases} f & f \leq f_c \\ f_c + \frac{f_u - f_c}{f_f - f_c} (f - f_c) & f > f_c \end{cases} \quad f_c \leq f_c \quad (9)$$

f_c is the critical void volume fraction at which void coalescence first occurs and f_f is the value at final failure. As the void volume fraction $f \rightarrow f_f$, the acceleration function $f^* \rightarrow f_u^* = 1/q_1$. To avoid numerical difficulties, $f \rightarrow 0.95f_f$ is used in Eq. (9), at which f is frozen implying local ductile material failure. Details of implementation in LE-VCFEM are given in Paquet et al. (2011a), Hu and Ghosh (2008).

2.1.3. Homogenization-based continuum plasticity-damage (HCPD) constitutive relations for level-0 elements

The rate dependent homogenization-based continuum plasticity-damage (HCPD) model for porous viscoplastic materials containing brittle inclusions is developed in Paquet et al. (2011), Dondeti et al. (2012) based on an anisotropic GTN model framework. The homogenized Cauchy stress rate is related to the elastic strain-rate tensor as:

$$\dot{\Sigma} = \bar{\mathbf{C}}^e : \dot{\epsilon}^e = \bar{\mathbf{C}}^e : (\dot{\epsilon} - \dot{\epsilon}^p) \quad (10)$$

where $\bar{\mathbf{C}}^e$ is a homogenized fourth order anisotropic elasticity tensor. The elastic anisotropy is due to the distribution of the inclusions. The total homogenized strain-rate is assumed to be additively decomposed into homogenized elastic and viscoplastic parts as $\dot{\epsilon} = \dot{\epsilon}^e + \dot{\epsilon}^p$. $\bar{\phi}$ is the loading surface in the stress space for the homogenized three-phase material (voids and inclusions in the matrix). Following the structure of GTN models in Gurson (1977), Tvergaard and Needleman (1984), Ghosh et al. (2009), the effective flow potential $\bar{\phi}$ in the HCPD model is expressed in terms of the hydrostatic (Σ^{hyd}) and deviatoric (Σ_{eq}) parts of the homogenized Cauchy stress tensor as:

$$\bar{\phi} = \left(\frac{\Sigma_{eq}}{\bar{\sigma}_c} \right)^2 + 2Q_1 \bar{f} \cosh \left(\frac{3Q_2}{2} \frac{\Sigma^{hyd}}{\bar{\sigma}_c} \right) - 1 - (Q_1 \bar{f})^2 = 0 \quad (11)$$

where \bar{f} is the homogenized void volume fraction. The parameters Q_1 and Q_2 are introduced to capture the effect of void interaction (Ghosh et al., 2009). The flow potential in Eq. (11) exhibits anisotropy emanating from two sources, viz. (i) dispersion of brittle inclusions in the matrix, and (ii) evolution of damage (voids) in the microstructure. Anisotropy is accounted for, through a homogenized equivalent stress Σ_{eq} following Hill's anisotropic yield function (Hill, 1948). Under plane strain condition, this is expressed as:

$$\Sigma_{eq}^2 = F(\Sigma_{yy} - \Sigma_{zz})^2 + G(\Sigma_{zz} - \Sigma_{xx})^2 + H(\Sigma_{xx} - \Sigma_{yy})^2 + C\Sigma_{xy}^2 \quad (12)$$

All variables in Eqs. (11) and (12) are expressed in an evolving, *material-damage principal (MDP) coordinate system*. In the MDP coordinate system, the material is assumed to retain its initial anisotropy (orthotropy in this case) throughout the deformation process. The orientation of the material-damage coordinate system is computed in each increment of the deformation process by enforcing the orthotropy condition as shown in Ghosh et al. (2009). The anisotropy parameters F, G, H and C have been found to be functions of the evolving plastic work W_p in the SERVE in Ghosh et al. (2009), Paquet et al. (2011).

In Eq. (11), $\bar{\sigma}_c$ corresponds to the averaged stress in the heterogeneous material consisting of matrix and inclusions, but without voids. The corresponding over-stress \bar{F} in the viscoplasticity flow rule (Perzyna, 1966) is expressed as:

$$\bar{F} = \bar{\sigma}_c - Y_f(W_p) \quad (13)$$

where Y_f is the rate-independent homogenized yield strength of the heterogeneous material without voids, which depends on the plastic work W_p . The homogenized viscoplastic strain-rate tensor, normal to the loading surface $\bar{\phi}(\bar{F})$ in the stress space, is derived as (Dondeti et al., 2012):

$$\dot{\mathbf{e}}^p = \dot{\lambda} \frac{\partial \bar{\phi}}{\partial \Sigma} = \frac{(1 - \bar{f})\bar{\sigma}_c}{\Sigma : \frac{\partial \bar{\phi}}{\partial \Sigma}} \Gamma_0 \Phi(\bar{F}) \frac{\partial \bar{\phi}}{\partial \Sigma} \quad (14)$$

$\dot{\lambda}$ is a homogenized viscoplastic multiplier obtained by enforcing the Hill-Mandel micro-macro energy equivalence condition in Hill (1972). Γ_0 is a temperature dependent viscosity coefficient and the function $\Phi(\bar{F})$ is chosen to be of the power law form $\langle \bar{F} \rangle^p$, where $\langle \rangle$ is the MacCauley operator. Finally, the evolution equations for the homogenized plastic work W_p , yield stress Y_f , and void volume fraction \bar{f} are expressed as:

$$\dot{W}_p = \Sigma : \dot{\mathbf{e}}^p, \quad \dot{Y}_f = \frac{\partial Y_f}{\partial W_p} \dot{W}_p, \quad \dot{\bar{f}} = \dot{\bar{f}}_{growth} + \dot{\bar{f}}_{nucleation} \quad (15)$$

where $\dot{\bar{f}}_{growth} = (1 - \bar{f})\dot{\mathbf{e}}^p_{kk}$. The homogenized void nucleation rate $\dot{\bar{f}}_{nucleation}$ follows directly from the inclusion cracking statistics in the underlying microstructural SERVE, that occurs in LE-VCFEM simulations. A strain-based homogenized void nucleation model is proposed in Dondeti et al. (2012), accounting for the effects of the underlying microstructural morphology and rate-dependency on damage nucleation. It invokes the Weibull statistics probability function that is used to initiate inclusion cracking in Eq. (1). The macroscopic nucleation probability function \bar{P}_{frag} is written in terms of the homogenized strain tensor and its rate, as well as the inclusion size v as:

$$\bar{P}_{frag}(v, \hat{e}, \dot{\hat{e}}) = 1 - \exp \left[-\frac{v}{v_0} \left(\frac{\hat{e}}{e_0(\dot{\hat{e}})} \right)^{m(\dot{\hat{e}})} \right] \quad (16)$$

where e_0 and m are the Weibull parameters and v_0 is a reference volume. The Weibull parameters are determined to

be functions of the strain-rate $\dot{\hat{e}}$, where $\hat{e} = \langle A(\theta_p)e_1 + B(\theta_p)e_2 + C(\theta_p)e_3 \rangle$ is an effective strain measure in terms of the macroscopic principal strains $e_i, i = 1, 2, 3$. The coefficients A, B and C are functions of direction of the maximum principal strain, represented by an angle θ_p in 2D.

The area fraction of cracked inclusions for a given strain-rate is expressed in terms of the probability density function of the inclusion size $p(v)$ and the probability of inclusion fragmentation $\bar{P}_{frag}(v, \hat{e}, \dot{\hat{e}})$. For a discrete size distribution in a finite sized SERVE, the area fraction is expressed as:

$$\rho_c(\hat{e}, \dot{\hat{e}}) = \sum_{i=1}^N \frac{v_i}{v_0} p(v_i) \left(1 - \exp \left[-\frac{v_i}{v_0} \left(\frac{\hat{e}}{e_0(\dot{\hat{e}})} \right)^{m(\dot{\hat{e}})} \right] \right) \quad (17)$$

N is the number of discrete inclusion sizes v_i in the probability density function $p(v) = \sum_{i=1}^N \delta(v - v_i)p(v_i)$, where $\delta(v - v_i)$ is the Dirac delta function. Eq. (17) yields the area fraction of cracked inclusions for a constant strain-rate. To account for variations in strain-rates, the rate of evolution of the area fraction of cracked inclusions ρ is assumed to be governed by the relation:

$$\dot{\rho} = \tilde{k}^\star \frac{d\rho_c(\hat{e}, \dot{\hat{e}})}{d\hat{e}} \dot{\hat{e}}, \quad \text{for } \tilde{k}^\star = \begin{cases} \tilde{k} & \text{if } \tilde{k} \geq 1 \\ 0 & \text{if } \tilde{k} < 1 \end{cases} \quad (18)$$

with $\tilde{k} = \frac{1-\rho}{1-\rho_c(\hat{e}, \dot{\hat{e}})}$. The factor \tilde{k}^\star accounts for the instantaneous change in strain-rate. The homogenized void nucleation law in Eq. (15) is then expressed as:

$$\dot{\bar{f}}_{nucleation} = V_p \dot{\rho} \quad (19)$$

V_p is a material parameter that relates the homogenized nucleated void volume fraction to the area fraction of cracked inclusions.

2.2. Computational sub-domain level-1 Ω_{l1}

The *level-1* subdomain is an intermediate computational level that is used to facilitate a switch-over from macroscopic analysis in *level-0* subdomains Ω_{l0} using the HCPD model, complete micromechanical analysis in *level-2* subdomains Ω_{l2} by LE-VCFEM. This subdomain is seeded in regions where macroscopic variables in *level-0* simulations have locally high gradients. *Level-1* subdomains serve as “transition or swing” regions, where macroscopic gradients as well as microscopic variables in the statistically equivalent RVE, are processed to assess whether homogenization holds. Two-level analysis similar to the FE^2 methods, involving the regularized macroscopic analysis and SERVE-based micromechanical analysis, is conducted in these subdomains. Major steps in *level-1* element computations are as follows.

- (1) Macroscopic finite element analysis using the HCPD constitutive model in Section 2.1, is performed and the macroscopic fields are updated.
- (2) LE-VCFEM based micromechanical analysis of the microstructural SERVE as shown in Fig. 1(b) is conducted as a post-processing operation with periodic

boundary conditions and applied strain tensor $\bar{\epsilon}$, obtained from the HCPD-based macroscopic analysis.

- (3) Appropriate criteria (e.g. violation of boundary periodicity) are developed and applied using the microstructural solution to signal transition from *level-1* to *level-2* elements.

Micromechanical LE-VCFEM analysis has been combined with the asymptotic expansion homogenization (AEH) theory in Ghosh et al. (2009); Paquet et al. (2011); Dondeti et al. (2012) to calculate the microstructural response of the SERVE Y when subjected to a homogenized strain history $\bar{\epsilon}$ and periodic conditions on the boundary ∂Y . Y -periodicity of any function in the SERVE is expressed as $\mathbf{f}(\mathbf{x}, \mathbf{y}) = \hat{\mathbf{f}}(\mathbf{x}, \mathbf{y} + \mathbf{k}\mathbf{Y})$, where \mathbf{k} represents a 2×2 array of integers. In an incremental formulation, the Y -periodic displacement conditions $\Delta u_i(\mathbf{x}, \mathbf{y}) = \Delta u_i(\mathbf{x}, \mathbf{y} + \mathbf{k}\mathbf{Y})$ are applied on ∂Y and the macroscopic strain $\bar{e}_{ij} + \Delta \bar{e}_{ij}$ is imposed on Y . To implement the AEH theory in conjunction with LE-VCFEM based micromechanical analysis, a modification of the formulation in Hu and Ghosh (2008), Paquet et al. (2011a) is needed for the energy functional in Y . The SERVE is tessellated into N Voronoi cell elements, each encompassing a region Y_e and comprised of a boundary ∂Y_e with outward normal \mathbf{n}^e . Furthermore the matrix-inclusion interface is delineated as ∂Y_c with outward normal \mathbf{n}^c , while the inclusion crack is ∂Y_{cr} with outward normal \mathbf{n}^{cr} . Increments of microscopic displacements on the element boundary ∂Y_e , inclusion-matrix interface ∂Y_c and crack boundary ∂Y_{cr} are represented by $\Delta \mathbf{u}$, $\Delta \mathbf{u}^c$, $\Delta \mathbf{u}^{cr}$ respectively. The corresponding incremental energy functional for each Voronoi cell element is written as Ghosh et al. (2009):

$$\begin{aligned} \Pi_e = & - \int_{Y_e \setminus Y_s} \frac{1}{2} S_{ijkl}^{tan} \Delta \sigma_{ij} \Delta \sigma_{kl} dY - \int_{Y_e \setminus Y_s} \epsilon_{ij} \Delta \sigma_{ij} dY \\ & + \int_{\partial Y_e} (\sigma_{ij} + \Delta \sigma_{ij})(u_i + \Delta u_i) n_j^e d\partial Y \\ & - \int_{\partial Y_c} (\sigma_{ij}^m + \Delta \sigma_{ij}^m - \sigma_{ij}^c - \Delta \sigma_{ij}^c)(u_i^c + \Delta u_i^c) n_j^c d\partial Y \\ & - \int_{\partial Y_{cr}} (\sigma_{ij}^c + \Delta \sigma_{ij}^c)(u_i^{cr} + \Delta u_i^{cr}) n_j^{cr} d\partial Y \\ & - \int_{Y_s} \frac{1}{2} E_{ijkl}^{tan} \Delta \epsilon_{ij}^s \epsilon_{kl}^s dY - \int_{Y_s} \sigma_{ij}^s \Delta \epsilon_{ij}^s dY \\ & + \int_{\partial Y_s} (\sigma_{ij}^s + \Delta \sigma_{ij}^s)(u_i^s + \Delta u_i^s) n_j^s d\partial Y \\ & + \int_{Y_e \setminus Y_s} (\bar{e}_{ij} + \Delta \bar{e}_{ij}) \Delta \sigma_{ij} dY + \int_{Y_s} (\bar{e}_{ij} + \Delta \bar{e}_{ij}) E_{ijkl}^{tan} \Delta \epsilon_{kl}^s dY \end{aligned} \quad (20)$$

All variables in Eq. (20) represent association with both scales, differentiated by a factor $\epsilon = \frac{x}{y} \ll 1$, where x and y correspond to macroscopic and microscopic length scales respectively. In LE-VCFEM Y_s is the region of displacement-based FE enrichment in regions of strain softening within each Voronoi cell element Y_e . Superscripts m, c, cr and s correspond to variables associated with the matrix, inclusion, crack and the enriched displacement-based finite element region in each Voronoi cell element respec-

tively. The microscopic equilibrated stress and strain increments are $\Delta \sigma$ and $\Delta \epsilon$ respectively. S_{ijkl}^{tan} and E_{ijkl}^{tan} are the instantaneous elastic-viscoplastic compliance and stiffness tensors respectively. The last two terms in Eq. (20) incorporate the effect of the applied macroscopic strain \bar{e}_{ij} .

The homogenized Cauchy stress Σ , total strain $\bar{\epsilon}$, rate of change of void volume fraction \dot{f} and plastic work W_p are obtained by volume-averaging respective variables over the SERVE as:

$$\begin{aligned} \Sigma_{ij} &= \frac{1}{Y} \int_Y \sigma_{ij}(\mathbf{y}) dY \quad (a) \\ \bar{e}_{ij} &= \frac{1}{Y} \int_Y \epsilon_{ij}(\mathbf{y}) dY + \frac{1}{2Y} \int_{\partial Y_{int}} ([u_i] n_j + [u_j] n_i) d\partial Y \quad (b) \\ \dot{f} &= \frac{1}{Y} \int_Y \dot{f} dY \quad (c) \\ W_p &= \frac{1}{Y} \int_Y \sigma_{ij} \dot{\epsilon}_{ij}^p \quad (d) \end{aligned} \quad (21)$$

where $\dot{\epsilon}^p$ is the microscopic plastic strain. The second term in Eq. (21)(b) corresponds to a discrete crack opening. Since the fracture in this model is represented parametrically, this term is omitted.

2.3. Computational sub-domain level-2 (Ω_{l2})

The sub-domain Ω_{l1} is replaced by *level-2* sub-domains Ω_{l2} , where micromechanical analysis of detailed microscopic regions is needed. The explicit morphology of the underlying microstructure is incorporated to be solved concurrently by the microstructural LE-VCFEM (Hu and Ghosh, 2008; Paquet et al., 2011a; Ghosh, 2011) in these regions. High resolution microstructure morphology is required to solve the micromechanical boundary value problem in Ω_{l2} . A method to reconstruct high resolution heterogeneous microstructures from limited micrograph information has been developed in Ghosh et al. (2006).

2.4. Computational sub-domain level-tr (Ω_{tr})

The interface between macroscopic *level-0/level-1* elements in $\Omega_{l0/l1}$ and *level-2* elements in Ω_{l2} with explicit morphology requires satisfaction traction and displacement continuity conditions. To facilitate smooth transition of scales across the disparate element boundaries, a layer of *level-tr* transition elements in Ω_{tr} is sandwiched between elements in *level-0/level-1* and *level-2* subdomains. Elements in Ω_{tr} are essentially *level-2* elements that have compatibility and traction continuity constraints imposed on their interface with *level-0/level-1* elements. Transition elements are located beyond the *level-2* regions, away from critical hot-spots. It has been shown in Ghosh (2011); Ghosh et al. (2007) that if displacement constraints are directly imposed on nodes of Voronoi cell finite elements in the transition elements for compatibility with the adjacent *level-1* elements, spurious stress concentrations arise at the interface. This has been averted by incorporating a relaxed, displacement-constraint method in Ghosh (2011); Ghosh et al. (2007). In this method, a weak form of the interface displacement continuity is implemented by using Lagrange multipliers. It relaxes the *level-0-transition* element inter-

face displacement constraint to satisfy compatibility in a weak sense as described in Section 4.

3. Mesh adaptivity and level change criteria

There are two classes of error leading to adaptivity in the proposed model. The first one is to reduce discretization error in the macroscopic scale due to inadequate refinement of the *level-0* mesh. This adaptation only refines the mesh to reduce error due to inappropriate FE discretization. The error could however be an implicit indicator of where high gradients in the solution exist and have the secondary benefit of identifying regions, which lack adequate resolution in the physics of the problem. The second adaptivity is to explicitly reduce modeling error due to inadequate representation of the physics of the problem through transcending scales. This leads to multi-scaling and level transitions. The mathematical development of rigorous bounds for discretization and modeling error for highly nonlinear problems with damage is very difficult and hence rare in the literature. Adaptation criteria used in this paper are developed from physical considerations.

3.1. Mesh refinement for *level-0* elements

Adaptive mesh refinement by *h*-adaptation of *level-0* elements is conducted to reduce the discretization error associated with critical variables in the solution. The *h*-adaptation procedure subdivides macroscopic elements into smaller elements to reduce a suitably chosen error, as well as to identify regions of modeling error by zooming in on regions with evolving gradients. The adaptation criterion is formulated in terms of the jump in traction across adjacent element boundaries (Ghosh et al., 2007), which is directly related to the local stress gradients (Bass and Oden, 1987). It states: Refine element e in Ω_{l0} if the traction jump error across the element boundary satisfies the condition:

$$E_e^{tj} \geq C_1 E_{max}^{tj} \quad \text{where}$$

$$E_{max}^{tj} = \max_e (E_e^{tj}) \quad \text{and} \quad (E_e^{tj})^2 = \frac{\int_{\partial\Omega_e} ([T_x]^2 + [T_y]^2) d\partial\Omega}{\int_{\partial\Omega_e} d\partial\Omega} \quad (22)$$

E_{max}^{tj} is the highest of all E_e^{tj} values for all *level-0* elements and the factor $C_1 < 1$ is chosen from numerical experiments. T_x and T_y are the boundary traction components in x and y directions and $[[\cdot]]$ is the jump operator across the element boundary $\partial\Omega_e$. This criterion also has the secondary benefit of identifying regions where damage is expected to localize expected due to local stress concentration and gradients.

3.2. Criteria for switching from *level-0* to *level-1* elements

The transition from *level-0* to *level-1* elements is aimed at identifying regions of departure from homogenizability, due to the intensity of local deformation and deformation gradients. For problems involving ductile deformation and damage, localization of macroscopic void volume fraction is an indicator of this departure, and hence, the transi-

tion criterion is developed in terms of void volume fraction \bar{f} and its gradients in Ω_{l0} . The transition of an element e in Ω_{l0} to Ω_{l1} is conditioned upon the criterion:

$$E_e^{gdf} f_e^* \geq C_2 E_{max}^{gdf} f_{max}^* \quad (23)$$

where $f^* = \frac{\bar{f} - \bar{f}_0}{\bar{f}_0}$ is the normalized void volume fraction with respect to the initial void volume fraction \bar{f}_0 . In Eq. (23), E_e^{gdf} is the norm of the local gradient of f^* expressed as:

$$E_e^{gdf} = \sqrt{\frac{\partial f_e^*}{\partial x}^2 + \frac{\partial f_e^*}{\partial y}^2} \quad (24)$$

The quantities f_{max}^* and E_{max}^{gdf} are the maximum values of all f^* and E_e^{gdf} . $C_2 < 1$ is a prescribed factor determined from numerical experiments. The gradient of f^* is computed by first interpolating over a patch of elements according to the Zienkiewicz-Zhu super-convergent patch recovery method (Zienkiewicz et al., 1992) and then differentiating.

3.3. Criteria for switching from *level-1* to *level-2* elements

Transition from *level-1* to *level-2* is activated for elements that fail the macroscopic uniformity and RVE periodicity tests. *Level-1* elements already correspond to those for which macroscopic nonuniformity has been established according to the criterion in Eq. (23). Subsequently, departure from RVE periodicity is used as an indicator for a switch from *level-1* to *level-2* elements. The switching criterion is developed in terms of a violation of the traction anti-periodicity condition in the microstructural SERVE, quantified as:

$$TR_e^{apt} = \frac{\left\| \sum_{i=1}^{NSGPR} \int_{\Gamma_i} \left(|t_x^{i+} + t_x^{i-}| \mathbf{i} + |t_y^{i+} + t_y^{i-}| \mathbf{j} \right) d\Gamma \right\|}{\max_e \left\| \sum_{i=1}^{NSEG} \int_{\Gamma_i} \left(|t_x^i| \mathbf{i} + |t_y^i| \mathbf{j} \right) d\Gamma \right\|} \quad (25)$$

$NSGPR$ is the number of boundary segment-pairs on the boundary of each SERVE (shown in Fig. 1(b)) over which the stresses should be anti-periodic and $NSEG$ is the total number of boundary segments on the SERVE. Traction t with superscripts + and - in the numerator correspond to those on the segment pairs with anti-periodicity conditions. The numerator is a measure of the residual traction violating the anti-periodicity condition. The denominator on the other hand corresponds to the maximum value of the absolute sum of all traction measures in all the SERVE's of *level-1* elements. TR_e^{apt} provides a measure of the lack of anti-periodicity of boundary tractions, since $TR_e^{apt} = 0$ if and only if the boundary tractions are anti-periodic. A *level-1* element e in Ω_{l1} is switched to a *level-2* microscopic element if:

$$TR_e^{apt} \geq C_3 \quad (26)$$

where $C_3 < 1$ is a constant determined from numerical experiments.

In addition, the *level-0/level-1* to *level-2* switching criterion is also activated for elements undergoing significant damage according to the criterion:

$$\rho_e \geq \rho_{crit} \quad \forall e \in \Omega_{l1} \quad (27)$$

where ρ_e is the area fraction of cracked inclusions in the SERVE of *level-1* element e . A value of $\rho_{crit} = 0.1$ has shown to significantly reduce the sensitivity of the solution to the parameter C_3 in Eq. (26).

3.3.1. Updating history-dependent state variables in transformed level-2 elements

Once the regions of *level-2* and *level-tr* elements have been identified, it is important to update the microstructural information within each newly created element. This includes the history of displacements, stress, elastic and plastic strains, and damage. It should be noted that a simple mapping of *level-0/level-1* variables onto *level-2* elements is not feasible. Their morphologies are very different, one being homogeneous and the other heterogeneous. Alternatively, the history of all state and internal variables in the microstructure are obtained by incrementally solving the local micromechanical LE-VCFEM boundary value problem for each *level-2* element from the start (increment 1) to the increment just before level transformation. The history of the macroscopic displacement solution on the *level-0/level-1* element boundary is utilized for this purpose. This macroscopic displacement history is applied as boundary conditions to the micromechanical LE-VCFEM problem for each *level-2* element.

The local micromechanical analysis precedes the coupled concurrent analysis of the current step. Once the history has been generated, the newly created *level-2* element is connected to the multi-scale mesh and a relaxation step is performed to recover local equilibrium.

4. Coupling multiple levels in the concurrent setting

Concurrent multi-scale analysis requires that all levels consisting of different sub-domains $\Omega_{l0}, \Omega_{l1}, \Omega_{l2}$, and Ω_{tr} be coupled and solved simultaneously. The global stiffness matrix and load vectors are derived for the entire computational domain $\Omega_{het} = \Omega_{l0} \cup \Omega_{l1} \cup \Omega_{l2} \cup \Omega_{tr}$. The corresponding domain boundary is partitioned as $\Gamma_{het} = \Gamma_{l0} \cup \Gamma_{l1} \cup \Gamma_{l2} \cup \Gamma_{tr}$, where $\Gamma_{l0} = \Gamma_{het} \cap \partial\Omega_{l0}$, $\Gamma_{l1} = \Gamma_{het} \cap \partial\Omega_{l1}$, $\Gamma_{l2} = \Gamma_{het} \cap \partial\Omega_{l2}$, and $\Gamma_{tr} = \Gamma_{het} \cap \partial\Omega_{tr}$. The continuity of displacements and tractions across the macro-scale sub-domain $\Omega_{l0} \cup \Omega_{l1}$ and micro-scale sub-domain $\Omega_{l2} \cup \Omega_{tr}$ is enforced using the relaxed, displacement-constraint method in Ghosh (2011); Ghosh et al. (2007). The method uses Lagrange multipliers to enforce (in a weak sense) continuity of displacements and tractions at the interface between macro-scale and micro-scale elements. The interface between these two modeling scales is denoted as $\Gamma_{int} = (\partial\Omega_{l0} \cup \partial\Omega_{l1}) \cap (\partial\Omega_{l2} \cup \partial\Omega_{tr})$.

4.1. Weak form for the concurrent multi-scale model

The principle of virtual work for Ω_{het} at the end of the increment $n+1$, associated with a virtual displacement field δu_i , is expressed as a sum of the individual contributions from each sub-domain as:

$$\delta\Pi_{het}^{n+1} = \delta\Pi_{\Omega_{l0}}^{n+1} + \delta\Pi_{\Omega_{l1}}^{n+1} + \delta\Pi_{\Omega_{l2}}^{n+1} + \delta\Pi_{\Omega_{tr}}^{n+1} + \delta\Pi_{\Gamma_{int}}^{n+1} = 0 \quad (28)$$

where

$$\begin{aligned} \delta\Pi_{\Omega_{l0}}^{n+1} &= \int_{\Omega_{l0}} (\Sigma_{ij}^{l0} + \Delta\Sigma_{ij}^{l0}) \frac{\partial\delta u_i^{l0}}{\partial x_j} d\Omega - \int_{\Gamma_{l0}} (t_i^{l0} + \Delta t_i^{l0}) \delta u_i^{l0} d\Gamma \\ \delta\Pi_{\Omega_{l1}}^{n+1} &= \int_{\Omega_{l1}} (\Sigma_{ij}^{l1} + \Delta\Sigma_{ij}^{l1}) \frac{\partial\delta u_i^{l1}}{\partial x_j} d\Omega - \int_{\Gamma_{l1}} (t_i^{l1} + \Delta t_i^{l1}) \delta u_i^{l1} d\Gamma \\ \delta\Pi_{\Omega_{l2}}^{n+1} &= \int_{\Omega_{l2}} (\sigma_{ij}^{l2} + \Delta\sigma_{ij}^{l2}) \frac{\partial\delta u_i^{l2}}{\partial x_j} d\Omega - \int_{\Gamma_{l2}} (t_i^{l2} + \Delta t_i^{l2}) \delta u_i^{l2} d\Gamma \\ \delta\Pi_{\Omega_{tr}}^{n+1} &= \int_{\Omega_{tr}} (\sigma_{ij}^{tr} + \Delta\sigma_{ij}^{tr}) \frac{\partial\delta u_i^{tr}}{\partial x_j} d\Omega - \int_{\Gamma_{tr}} (t_i^{tr} + \Delta t_i^{tr}) \delta u_i^{tr} d\Gamma \end{aligned}$$

$$\begin{aligned} \delta\Pi_{\Gamma_{int}}^{n+1} &= \delta \int_{\Gamma_{int}} (\lambda_i^{l0/l1} + \Delta\lambda_i^{l0/l1})(v_i + \Delta v_i - u_i^{l0/l1} - \Delta u_i^{l0/l1}) d\Gamma \\ &\quad + \delta \int_{\Gamma_{int}} (\lambda_i^{tr} + \Delta\lambda_i^{tr})(v_i + \Delta v_i - u_i^{tr} - \Delta u_i^{tr}) d\Gamma \end{aligned}$$

In the functional Π_{het}^{n+1} (28), superscripts $l0, l1, l2$, and tr associate the variables to their respective sub-domain. Variables in Π_{het}^{n+1} are evaluated at the end of the increment $n+1$, i.e. $(\cdot)^{n+1} = (\cdot)^n + (\Delta \cdot)^{n+1}$ where the prefix ' Δ ' denotes increments of the respective variables in the incremental solution process. The multi-level functional in Eq. (28) couples macro-scale fields such as stresses $\Sigma_{ij}^{l0/l1}$, tractions $t_i^{l0/l1}$ and displacements $u_i^{l0/l1}$ in $\Omega_{l0} \cup \Omega_{l1}$ with their micro-scale counterparts $\sigma_{ij}^{l2/tr}, t_i^{l2/tr}$ and $u_i^{l2/tr}$ in $\Omega_{l2} \cup \Omega_{tr}$ through the term $\Pi_{\Gamma_{int}}^{n+1}$ associated with Lagrange multipliers $\lambda_i^{l0/l1}$ and λ_i^{tr} corresponding to macro-scale and micro-scale variables at the interface Γ_{int} respectively. The stress $\Sigma_{ij}^{l0/l1}$ is the homogenized macroscopic stress in Ω_{l0} and Ω_{l1} , while the stress $\sigma_{ij}^{l2/tr}$ is obtained from LE-VCFEM solution of the microstructural regions Ω_{l2} and Ω_{tr} . $u_i^{l0}, u_i^{l1}, u_i^{l2}$, and u_i^{tr} are displacement degrees of freedom of elements in the $\Omega_{l0}, \Omega_{l1}, \Omega_{l2}$, and Ω_{tr} sub-domains respectively. Tractions $t_i^{l0}, t_i^{l1}, t_i^{l2}$, and t_i^{tr} are prescribed on the boundaries $\Gamma_{l0}, \Gamma_{l1}, \Gamma_{l2}$, and Γ_{tr} respectively. On each segment of Γ_{int} , the displacement field v_i is interpolated using a suitable polynomial function, independent of the interpolations on $\partial\Omega_{l0}, \partial\Omega_{l1}, \partial\Omega_{l2}$, and $\partial\Omega_{tr}$. The functional $\Pi_{\Gamma_{int}}^{n+1}$ is used to enforce displacement continuity and traction reciprocity on Γ_{int} in a weak sense using $\lambda_i^{l0/l1}$ and λ_i^{tr} , which are vector columns of macro-scale and micro-scale Lagrange multipliers respectively. The Euler equations obtained by setting the coefficients of $\delta\lambda_i^{l0/l1}$ and $\delta\lambda_i^{tr}$ to zero respectively in Eq. (28) are:

$$\begin{aligned} \text{Coefficient of } \delta\lambda_i^{l0/l1} : u_i^{l0/l1} + \Delta u_i^{l0/l1} &= v_i + \Delta v_i \text{ on } \Gamma_{int} \\ \text{Coefficient of } \delta\lambda_i^{tr} : u_i^{tr} + \Delta u_i^{tr} &= v_i + \Delta v_i \text{ on } \Gamma_{int} \end{aligned} \quad (29)$$

These correspond to displacement continuity across Γ_{int} . Continuity of tractions across Γ_{int} is obtained by setting the coefficients of $\delta v_i, \delta u_i^{l0/l1}$, and δu_i^{tr} to zero:

$$\begin{aligned} \text{Coefficient of } \delta v_i : \lambda_i^{l0/l1} + \Delta\lambda_i^{l0/l1} \\ = -(\lambda_i^{tr} + \Delta\lambda_i^{tr}) \text{ on } \Gamma_{int} \end{aligned} \quad (30)$$

$$\begin{aligned} \text{Coefficient of } \delta u_i^{l0/l1} : \lambda_i^{l0/l1} + \Delta\lambda_i^{l0/l1} \\ = (\Sigma_{ij}^{l0/l1} + \Delta\Sigma_{ij}^{l0/l1}) n_j^{l0/l1} \text{ on } \Gamma_{int} \end{aligned}$$

Coefficient of $\delta u_i^{tr} : \lambda_i^{tr} + \Delta \lambda_i^{tr} = (\sigma_{ij}^{tr} + \Delta \sigma_{ij}^{tr}) n_j^{tr}$ on Γ_{int}

where n_j is the unit normal vector and $\lambda_i^{l0/l1}$ and λ_i^{tr} correspond to the interfacial traction components on $\partial\Omega_{l0/l1} \cap \Gamma_{int}$ and $\partial\Omega_{tr} \cap \Gamma_{int}$ respectively. The Euler equations resulting from setting the coefficients of $\delta u_i^{l0/l1}$ and $\delta u_i^{l2/tr}$ to zero lead to the equilibrium equation within each sub-domains and traction continuity conditions between the sub-domains.

$$\begin{bmatrix} \mathbf{K}_{l0/l1}^{l,l} & \mathbf{K}_{l0/l1}^{l,O} & 0 & 0 & 0 & \mathbf{P}_{l0/l1} & 0 \\ \mathbf{K}_{l0/l1}^{O,l} & \mathbf{K}_{l0/l1}^{O,O} & 0 & 0 & 0 & 0 & 0 \\ 0 & 0 & \mathbf{K}_{tr}^{l,l} & \mathbf{K}_{l2/tr}^{l,O} & 0 & 0 & \mathbf{P}_{tr} \\ 0 & 0 & \mathbf{K}_{l2/tr}^{O,l} & \mathbf{K}_{l2/tr}^{O,O} & 0 & 0 & 0 \\ 0 & 0 & 0 & 0 & 0 & \mathbf{Q}_{l0/l1} & \mathbf{Q}_{tr} \\ \mathbf{P}_{l0/l1}^T & 0 & 0 & 0 & \mathbf{Q}_{l0/l1}^T & 0 & 0 \\ 0 & 0 & \mathbf{P}_{tr}^T & 0 & \mathbf{Q}_{tr}^T & 0 & 0 \end{bmatrix}^i \begin{Bmatrix} \Delta \mathbf{q}_{l0/l1}^l \\ \Delta \mathbf{q}_{l0/l1}^O \\ \Delta \mathbf{q}_{tr}^l \\ \Delta \mathbf{q}_{l2/tr}^O \\ \Delta \mathbf{q}_{int} \\ \Delta \Lambda_{l0/l1} \\ \Delta \Lambda_{tr} \end{Bmatrix}^i = \begin{Bmatrix} \Delta \mathbf{F}_{l0/l1}^l \\ \Delta \mathbf{F}_{l0/l1}^O \\ \Delta \mathbf{F}_{tr}^l \\ \Delta \mathbf{F}_{l2/tr}^O \\ \Delta \mathbf{F}_{int} \\ \Delta \mathbf{F}_{l0/l1} \\ \Delta \mathbf{F}_{tr} \end{Bmatrix} \quad (37)$$

4.2. Finite element discretization for multi-scale analysis

Displacements v_i and the Lagrange multipliers $\lambda_i^{l0/l1}$ and λ_i^{tr} are interpolated from nodal values using suitable shape functions as:

$$\{\mathbf{v}\} = [\mathbf{L}_{int}]\{\mathbf{q}_{int}\} \quad (31)$$

$$\{\lambda^{l0/l1}\} = [\mathbf{L}_{\lambda^{l0/l1}}]\{\Lambda_{l0/l1}\} \quad (32)$$

$$\{\lambda^{tr}\} = [\mathbf{L}_{\lambda^{tr}}]\{\Lambda_{tr}\} \quad (33)$$

The displacements u_i^{l0} and u_i^{l1} in each level-0 and level-1 elements are interpolated with the standard Legendre polynomials based shape functions as:

$$\{\mathbf{u}^{l0}\} = [\mathbf{N}_{l0}]\{\mathbf{q}_{l0}\} = [\mathbf{N}_{l0}^l \mathbf{N}_{l0}^O] \begin{Bmatrix} \mathbf{q}_{l0}^l \\ \mathbf{q}_{l0}^O \end{Bmatrix} \quad (34)$$

$$\{\mathbf{u}^{l1}\} = [\mathbf{N}_{l1}]\{\mathbf{q}_{l1}\} = [\mathbf{N}_{l1}^l \mathbf{N}_{l1}^O] \begin{Bmatrix} \mathbf{q}_{l1}^l \\ \mathbf{q}_{l1}^O \end{Bmatrix} \quad (35)$$

The nodal displacements in level-0 and level-1 elements are partitioned into two sets. Those for nodes in $\Omega_{l0/l1}$ lying on the interface Γ_{int} are denoted as $\mathbf{q}_{l0/l1}^l$, while the other degrees of freedom are $\mathbf{q}_{l0/l1}^O$.

4.3. Iterative solution of the coupled multi-scale system

An iterative solver is used to solve the nonlinear algebraic equations obtained from the weak forms in Eq. (28) by setting the residual $\mathbf{R} = 0$. In a Newton–Raphson iterative solver, the i -th update of q_i at increment $n+1$ can be obtained from the linearized form:

$$\mathbf{R}^{n+1} = (\mathbf{R}^{n+1})^i + \frac{\partial \mathbf{R}}{\partial q_i} \Delta q_i = 0 \quad (36)$$

In the present work, a Quasi-Newton iterative solver, specifically the BFGS solver, is used to solve Eq. (36). For a given increment, the stiffness matrix $\frac{\partial \mathbf{R}}{\partial q_i}$ is evaluated only once, at the beginning of the iterative process. Introducing Eqs. (31)–(35)) into Eq. (36) and taking derivatives, yields the system of algebraic equations to be solved for the generalized degrees of freedom q_i (Ghosh et al., 2007):

The superscript I in Eq. (37) is associated with nodes lying on Γ_{int} , while O is associated with all other nodes. The use of two superscripts separated by a comma indicates the coupling effect. The stiffness sub-matrix $[\mathbf{K}_{l0/l1}]$ and sub-vector $\{\mathbf{F}_{l0/l1}\}$ for level-0 and level-1 elements are derived as:

$$\begin{aligned} (K_{l0/l1})_{mzn\beta} &= \int_{\Omega_{l0} \cup \Omega_{l1}} \frac{\partial N_\alpha}{\partial x_k} \frac{\partial \Sigma_{mn}}{\partial e_{kl}} \frac{\partial N_\beta}{\partial x_l} d\Omega (\Delta F_{l0/l1})_{m\alpha} \\ &= \int_{\Gamma_t} (t_m + \Delta t_m) N_\alpha d\Gamma + \int_{\Gamma_{int}} (\lambda_m + \Delta \lambda_m) N_\alpha d\Gamma \\ &\quad - \int_{\Omega_{l0} \cup \Omega_{l1}} (\Sigma_{mn} + \Delta \Sigma_{mn}) \frac{\partial N_\alpha}{\partial x_n} d\Omega \end{aligned} \quad (38)$$

Subscripts (m, n) are associated with degrees of freedom, while (α, β) correspond to node numbers in the element. These matrices and vectors are partitioned based on the corresponding I and O nodes. Coupling between the level-0 and level-1 elements with level-2 and level-tr elements is assured by the matrices $[\mathbf{P}]$ and $[\mathbf{Q}]$ defined as:

$$(P_{l0/l1})_{mzn\beta} = - \int_{\Gamma_{int}} N_{mz}^T (L_{\lambda^{l0/l1}})_{n\beta} d\Gamma \quad (39)$$

$$(P_{tr})_{mzn\beta} = - \int_{\Gamma_{int}} N_{mz}^T (L_{\lambda^{tr}})_{n\beta} d\Gamma$$

$$(Q_{l0/l1})_{mzn\beta} = \int_{\Gamma_{int}} (L_{int}^T)_{mz} (L_{\lambda^{l0/l1}})_{n\beta} d\Gamma$$

$$(Q_{tr})_{mzn\beta} = \int_{\Gamma_{int}} (L_{int}^T)_{mz} (L_{\lambda^{tr}})_{n\beta} d\Gamma \quad (40)$$

with their corresponding residual vectors $\{\mathbf{F}\}$, defined as:

$$\begin{aligned} (\Delta F_{int})_{m\alpha} &= - \int_{\Gamma_{int}} (L_{int}^T)_z (\lambda^{l0/l1} + \Delta \lambda^{l0/l1})_m d\Gamma \\ &\quad - \int_{\Gamma_{int}} (L_{int}^T)_z (\lambda^{tr} + \Delta \lambda^{tr})_m d\Gamma \end{aligned} \quad (41)$$

$$\begin{aligned}
 (\Delta F_{\lambda^{10/11}})_{m\alpha} &= - \int_{\Gamma_{int}} (L_{\lambda^{10/11}}^T)_\alpha [v_m + \Delta v_m] d\Gamma \\
 &\quad + \int_{\Gamma_{int}} (L_{\lambda^{10/11}}^T)_\alpha [(u_{10/11})_m + \Delta(u_{10/11})_m] d\Gamma \\
 (\Delta F_{\lambda^{tr}})_{m\alpha} &= - \int_{\Gamma_{int}} (L_{\lambda^{tr}}^T)_\alpha [v_m + \Delta v_m] d\Gamma \\
 &\quad + \int_{\Gamma_{int}} (L_{\lambda^{tr}}^T)_\alpha [(u_{tr})_m + \Delta(u_{tr})_m] d\Gamma
 \end{aligned}$$

Finally, the stiffness sub-matrix and load sub-vector associated with *level-2* and *level-tr* elements are obtained from LE-VCFEM calculations followed by a static condensation to retain the boundary terms only.

5. Numerical studies and validations

Numerical studies are undertaken to: (a) analyze the effect of the interface Γ_{int} on the solution, (b) to demonstrate the capabilities of the level-change criteria, and (c) to validate the multi-scale model for a problem for which a complete micromechanical analysis is tractable.

5.1. Effect of interface Γ_{int} between macro and micro sub-domains

This study investigates the effect of the order p of polynomial shape functions used to interpolate displacement \mathbf{v} on Γ_{int} . Appropriate shape functions must be used in the interpolation Eq. (31) to ensure that the interface retains accuracy with respect to microscopic displacements, stresses, and strains in $\Omega_{12} \cup \Omega_{tr}$. Two different microstructures with dimensions $48 \mu\text{m} \times 96 \mu\text{m}$ in the x and y directions are considered for this demonstration. Uniaxial tension in the y direction is applied by prescribing the following boundary conditions:

$$U_y = \Delta U \text{ at } y = 96 \mu\text{m}, U_y = 0 \text{ at } y = 0, U_x = 0 \text{ at } x = 0.$$

The computational domain is discretized into $248 \mu\text{m} \times 48 \mu\text{m}$ macro-scale. The two underlying microstructures of aluminum matrix containing silicon inclusions analyzed are:

- (1) A single elliptical inclusion of volume fraction $V_f = 10\%$, aspect ratio $\alpha = 2.0$, and orientation $\theta = 108.8^\circ$ with respect to the horizontal axis, in the square element.
- (2) Distributed microstructure from the micrograph of cast aluminum alloy.

The reference solutions are obtained by solving the micromechanical problem with LE-VCFEM, for which the material parameters are given in Section 5.3. Inclusion cracking is not considered in this study. The multi-level computational domain is comprised of one *level-0* macroscopic element (top element) that uses a homogenized constitutive model and one microscopic *level-tr* element (bottom element). The polynomial order p is varied from linear ($p = 1$) to quartic ($p = 4$). The microscopic stress field obtained from the multi-level analysis is compared with the micromechanical LE-VCFEM solution.

The microscopic stress σ_{yy} along the middle section, obtained for $\Delta U = 0.192 \mu\text{m}$ with the micromechanical and multi-level models with Γ_{int} modeled by ($p = 1, 4$) polynomial shape functions, are plotted in Fig. 2(a) and 2(b) for the two microstructures. Contour plots of σ_{yy} for the micromechanical and multi-scale analyses are also shown in Figs. 3 and 4. These numerical results show that while higher order polynomials lead to a better continuity of stresses across the interface, the resulting stress field is not necessarily more accurate in comparison with lower order interfaces. The linear interface ($p = 1$) representation is deemed to adequately represent the interface in the relaxed displacement constraint method and is henceforth adopted.

5.2. Calibration and validation of the level-1 to level-2 criteria

This set of examples calibrates and validates the criteria in Section 3.3 for identifying *level-1* elements that should be switched to *level-2* elements. The geometry of the problem considered is a square plate with a square hole in its center with dimensions shown in Fig. 5(a). Only one quarter of the plate is modeled and appropriate symmetry boundary conditions are prescribed. In addition to the symmetry boundary conditions, a total prescribed displacement ΔU_A is applied in the x direction on the left edge ($x = 0$) of the plate. The bottom of the plate $y = 0$ is free of any prescribed displacement and no traction boundary conditions are applied. The silicon inclusion and aluminum matrix parameters used for rate-independent micromechanical LE-VCFEM analysis are listed in Table 1 and Table 2 respectively. The plastic hardening behavior of the aluminum matrix without voids and without inclusions is plotted in Fig. 6.

First, the reference solution is obtained by solving a complete micromechanical analysis for the entire plate with *level-2* elements corresponding to the SERVE in Fig. 5(c). The next simulation models all macroscopic elements as *level-1* elements in a fully coupled FE² first-order homogenization scheme. At each increment, the value of TR_e^{apt} in Eq. (25) is computed for each element and stored. Evolution of TR_e^{apt} is then compared with the evolution of microstructural damage in the microscopic computational domain of LE-VCFEM analysis. Contour plots of TR_e^{apt} obtained with the homogenization scheme are shown in Fig. 7 for a total applied displacement of $U_A = -2.6 \mu\text{m}$. The corresponding contour plots of the microscopic stress component σ_{xx} , obtained by micromechanical analysis are also shown. These contour plots demonstrate that TR_e^{apt} successfully identifies the regions where macroscopic non-uniformities arise. To ascertain a value for C_3 in Eq. (26), contour plots of σ_{xx} for the multi-level model are compared with those for the fully micromechanical analysis. Two different values for C_3 are considered, viz. $C_3 = 0.08$ and 0.10 . The contour plots of σ_{xx} at $U_A = -2.6 \mu\text{m}$ obtained by the multi-level simulations in Fig. 8(a) and (b) are compared with those for the micromechanical analysis in Fig. 7. $C_3 = 0.08$ gives a good agreement with the micromechanical results. The Figs. 8(a) and (b) indicate a strong sensitivity of the solution to the selected value C_3 in Eq. (26). To mitigate this sensitivity

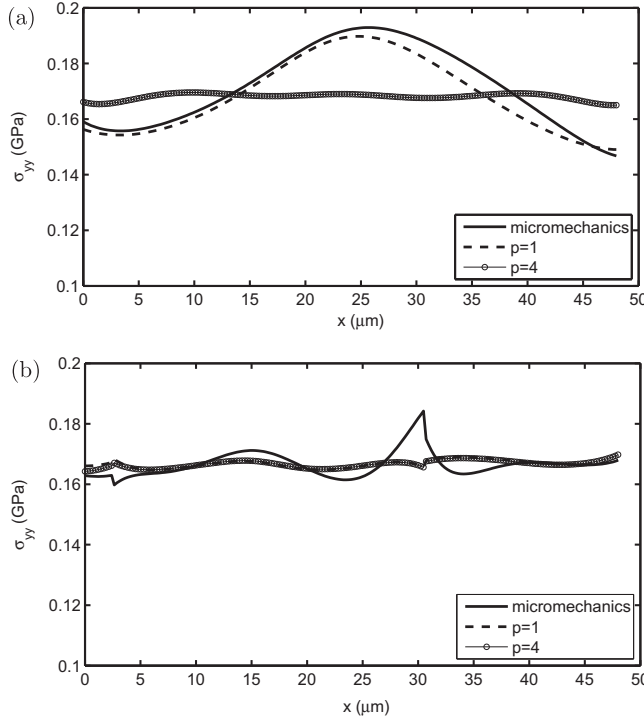


Fig. 2. Microscopic stress σ_{yy} (GPa) distribution along the interface Γ_{int} for the micromechanical and multi-scale analyses: (a) single inclusion microstructure, and (b) distributed aluminum microstructure.

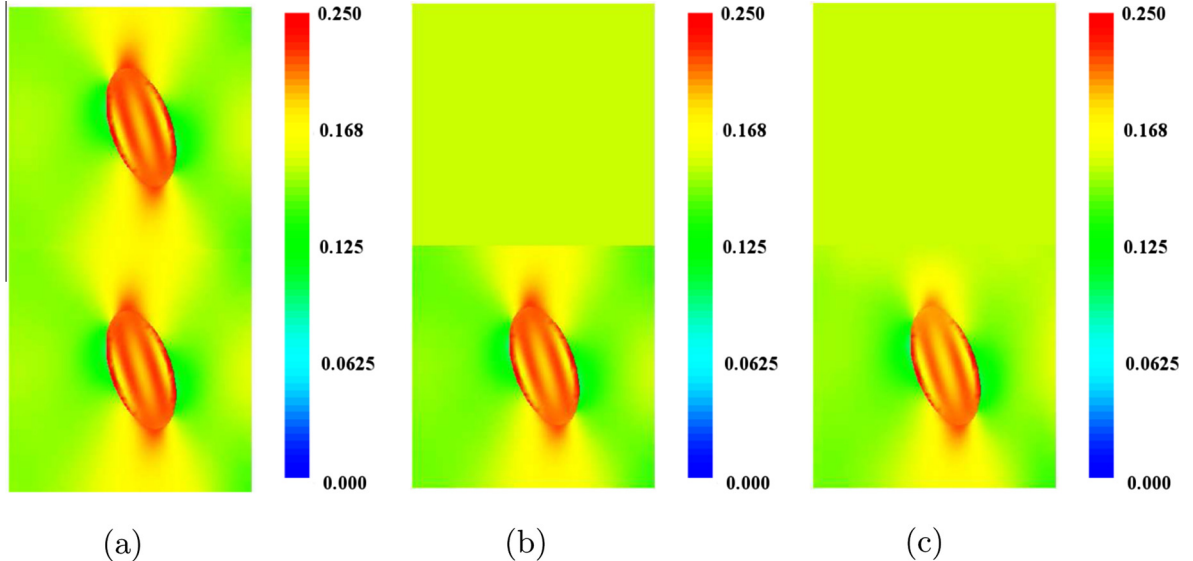


Fig. 3. Contour plot of microscopic stress component σ_{yy} (GPa) for the single inclusion microstructure by: (a) micromechanical analysis, (b) multi-level analysis with $p = 1$, and (c) multi-level analysis with $p = 4$.

in the multi-level analysis, Eq. (27) is also activated for this level change. A value $\rho_{crit} = 0.1$ increases the robustness of the multi-scale model by reducing the sensitivity of the solution to the parameter C_3 . This is shown in Fig. 8(c) for multi-level analysis with $C_3 = 0.10$ and $\rho_{crit} = 0.10$. Good agreement is found between these results and those

for the micromechanical analysis in Fig. 7. The combination of criteria (26) and (27) makes the multi-scale algorithm very reliable and accurate.

Finally to validate the effectiveness of Eqs. (26) and (27), the multi-level model is solved for the boundary value problem of cast aluminum alloy in Fig. 5. The

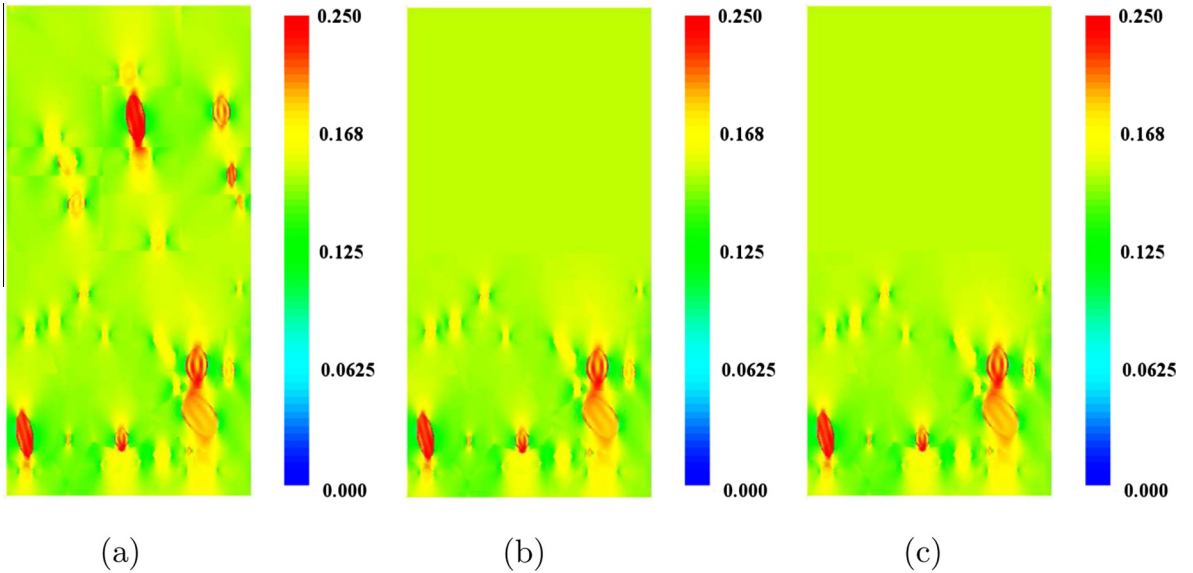


Fig. 4. Contour plot of microscopic stress component σ_{yy} (GPa) for the distributed aluminum alloy microstructure by: (a) micromechanical analysis, (b) multi-level analysis with $p = 1$, and (c) multi-level analysis with $p = 4$.

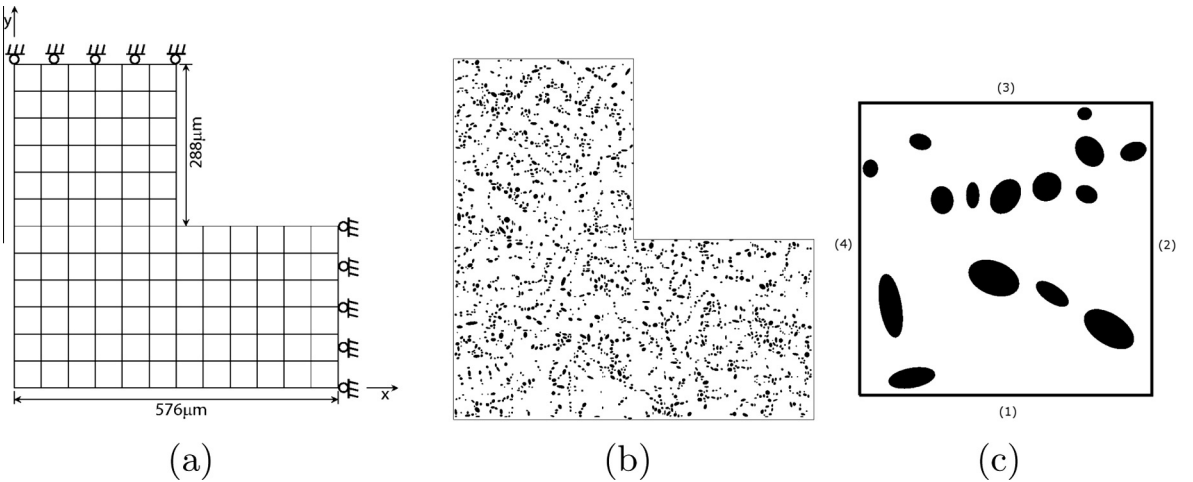


Fig. 5. (a) Geometry of the square plate with a center square hole, with applied symmetry boundary conditions, (b) underlying microstructure taken from a micrograph of a W319 cast aluminum alloy, and (c) statistically equivalent representative volume element (SERVE) ($48 \mu\text{m} \times 48 \mu\text{m}$).

Table 1
Inclusion elastic and cracking properties used in LE-VCFEM simulations.

| E (GPa) | v | σ_w (MPa) | m | ν_0 (μm^2) | P_{frag}^{cr} (%) |
|-----------|------|------------------|-----|-----------------------------|---------------------|
| 165 | 0.27 | 680 | 2.4 | 8.29 | 55 |

microstructure is taken from a micrograph in Fig. 5(b). Fig. 9 shows the contour plot of the microscopic stress σ_{xx} for an applied displacement $U_A = -4.32 \mu\text{m}$ by the adaptive multi-level model and a micromechanical simulation. The two results agree very well, which confirms the effectiveness of the multi-level model in predicting ductile fracturing.

Table 2
Aluminum matrix elastic, plastic and void evolution properties used in LE-VCFEM simulations.

| E (GPa) | v | γ_0 ($\text{GPa}^{-1} \text{s}^{-1}$) | p | f_0 | f_c | f_f | ϵ_N | s_N | f_N |
|-----------|------|--|-----|-------|-------|-------|--------------|-------|-------|
| 70 | 0.35 | 8.086 | 1 | 0.01 | 0.15 | 0.25 | 0.2 | 0.075 | 0.08 |

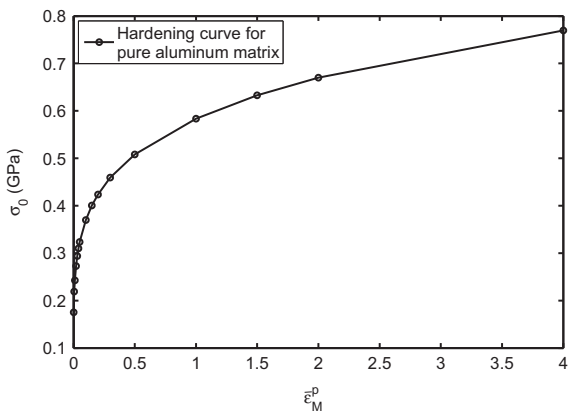


Fig. 6. Stress–strain behavior of the aluminum matrix used in LE-VCFEM simulations.

5.3. Validation of the multi-level model against micromechanical analysis

This study tests the accuracy of the multi-level model in simulating ductile fracture by comparing its predictions with those obtained by a LE-VCFEM-based micromechanical analysis. The macroscopic computational domain, a L-shaped connector link subjected to bending forces, is discretized into 108 QUAD4 elements as shown in Fig. 5(a). The underlying microstructure is kept simple for ease of micromechanical analysis by LE-VCFEM. Each macro-scale element is assumed to comprise a single silicon inclusion of volume fraction $V_f = 10\%$, aspect ratio $\alpha = 2.0$, and orientation $\theta = 0^\circ$ with respect to the horizontal axis, embedded in a square aluminum matrix (this constitutes the RVE too). Material parameters for individual phases are

reported in Tables 3 and 4 and the plastic hardening curve of the aluminum matrix is shown in Fig. 6. Rate effects are not considered in this example. The prescribed boundary conditions are: $U_x = -\Delta U$ at $y = 576 \mu\text{m}$, $U_x = 0$ at $x = 576 \mu\text{m}$, and $U_y = 0$ at $(x, y) = (576 \mu\text{m}, 0)$, where ΔU is incremented till fracture.

Results of multi-scale analysis by the multi-level and micromechanical models are depicted in the Figs. 10 and 11. Fig. 10(b) shows the evolved multi-level mesh at the end of the loading sequence. When the homogenized stress in a level-2 element decreases sharply, it indicates rapid propagation of microstructural damage in the matrix. At total failure, the level-2 element is replaced by a sealed macroscopic element (black elements in Fig. 10(a)) with near-zero constant stresses. This sealing feature in the wake of a crack significantly speeds up the multi-level simulations. Fig. 10(a) shows a comparison of the total reaction force at the fixed edge $x = 576 \mu\text{m}$ as a function of the applied displacement U_x by the multi-level and micromechanical simulations. A very good match is obtained between the two models. Each drop in the multi-level model results from failure of the underlying level-2 microstructure and sealing with macroscopic elements. Contour plots of void volume fraction f and equivalent plastic strain $\bar{\epsilon}_M^p$ by the two methods at final fracture are shown in the Figs. 11. The two contour plots in Figs. 11(b) and (c) concur in predicting the ductile crack path in the underlying microstructure. The contour plots for the multi-level model shows some discontinuities due to the element sealing process. This example demonstrates the accuracy of the multi-level model for solving the multi-scale ductile fracture problems.

As a concluding example, the effect of loading rates on ductile fracture is investigated. For this, the boundary value problem is solved for two different loading rates,

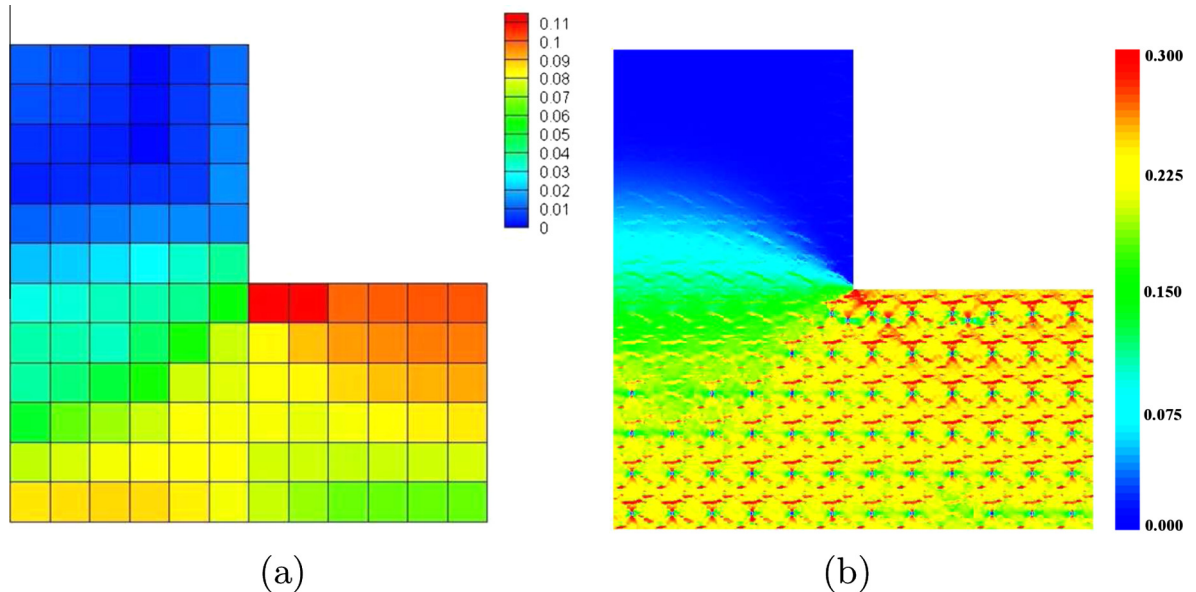


Fig. 7. Contour plot of TR_e^{opt} indicating the intensity of departure from traction anti-periodicity within each element of the fully macroscopic level-1 simulation and the corresponding contour plot of σ_{xx} (GPa) for the fully microscopic level-2 simulation: (a) TR_e^{opt} at $U_A = -2.6 \mu\text{m}$, (b) σ_{xx} at $U_A = -2.6 \mu\text{m}$.

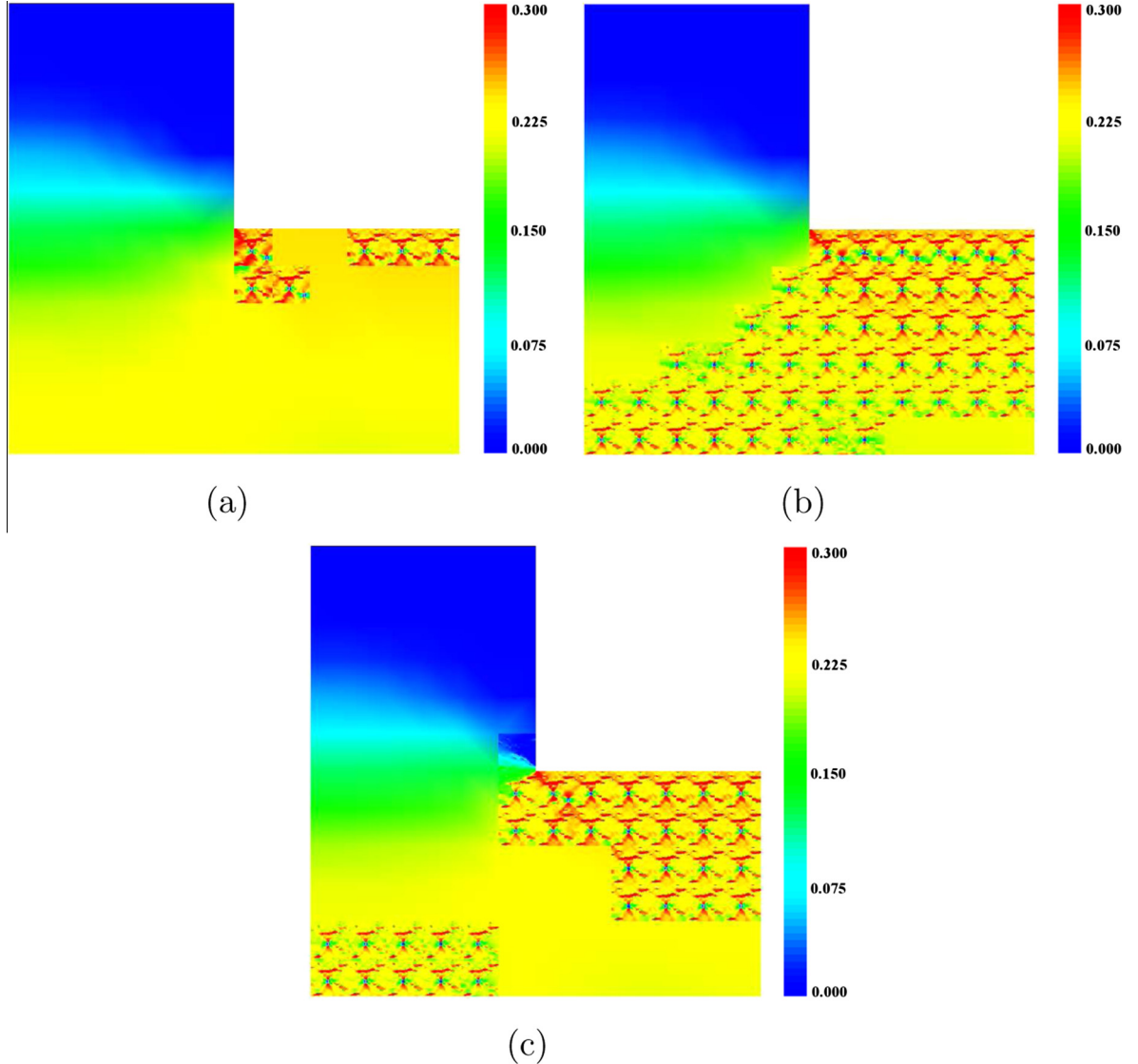


Fig. 8. Microscopic stress component σ_{xx} (GPa) with $U_A = -2.6 \mu\text{m}$, for which transition from level-1 to level-2 elements occurs at: (a) $TR_e^{opt} = 0.10$, (b) $TR_e^{opt} = 0.08$, and (c) $TR_e^{opt} = 0.10$ and $\rho > 0.10$.

corresponding to prescribed velocities $\dot{U}_x = -1.5 \mu\text{m/s}$ and $\dot{U}_x = -15.0 \mu\text{m/s}$ respectively. Fig. 12(c) shows the corresponding force-displacement response. For the higher rate, the total applied displacement at final fracture is significantly higher even though the high strain-rate in the microstructure result in early inclusion cracking. This increase of ductility is attributed to stress redistribution that delays the evolution of plasticity in the neighborhood of the cracked inclusions, thus reducing void nucleation and growth rates in those regions. Contour plots showing the distributions of the equivalent plastic strain in the microstructure for the two rates, are shown in Fig. 12(a) and (b). The viscoplastic response of the ductile matrix induces higher stresses in the silicon inclusions, resulting in a distribution of damage that is much more diffuse in comparison with the rate-independent behavior of the structure.

This indicates a strong sensitivity of the ductile behavior to the applied loading rate.

6. Ductile failure of a cast aluminum tension bar

The multi-level model is now applied for multi-scale ductile fracture analysis of an Al-Si-Mg cast aluminum alloy W319 rectangular bar, for which the micrograph is shown in Fig. 1(a). It comprises age-hardened ductile aluminum matrix, strengthened by Mg/Si and a dispersion of brittle Si particulates. Dimensions of the rectangular computational domain are: $384 \mu\text{m} \times 1536 \mu\text{m}$ in the horizontal (x) and vertical (y) directions respectively. High resolution microstructure of the alloy is mapped on the rectangular specimen following procedures detailed in Ghosh et al. (2006). Since it is impossible to analyze the

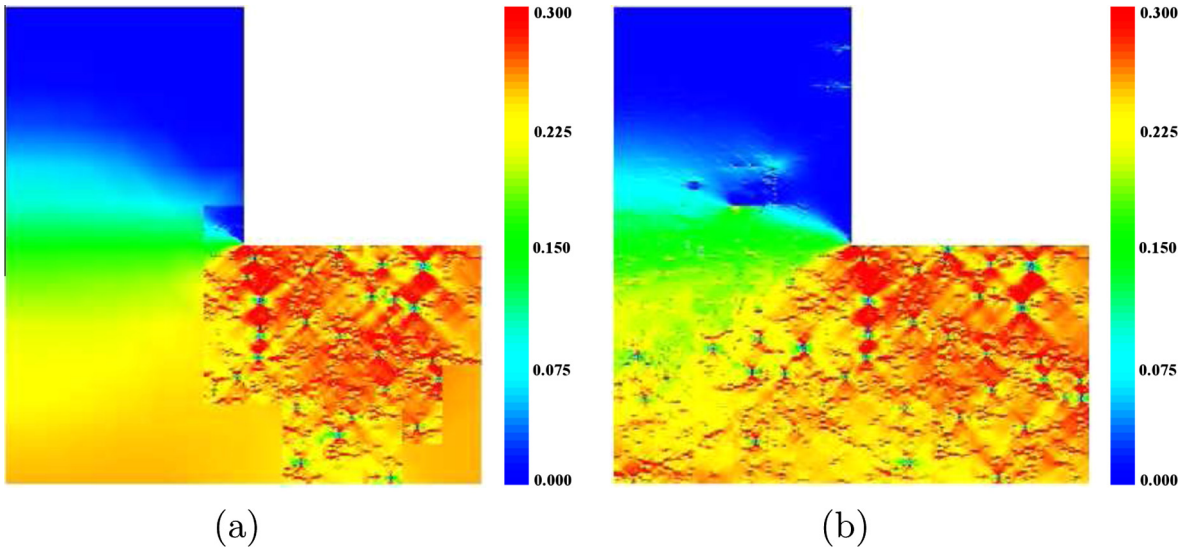


Fig. 9. Microscopic stress σ_{xx} (GPa) for an applied displacement $U_A = -4.32 \mu\text{m}$ by: (a) adaptive multi-level simulation with $TR_e^{\text{opt}} = 0.10$ and $\rho > 0.10$, and (b) fully micromechanical simulation.

Table 3
Inclusion elastic and cracking properties used in LE-VCFEM simulations.

| E (GPa) | ν | σ_w (MPa) | m | v_0 (μm^2) | $P_{\text{frag}}^{\text{cr}}$ (%) |
|-----------|-------|------------------|-----|---------------------------|-----------------------------------|
| 165 | 0.27 | 300 | 2.4 | 230.4 | 95 |

entire domain using a micromechanics model, the multi-level model is initiated with a *level-0* computational domain Ω_{l0} for the entire bar. The specimen is discretized into

Table 4
Aluminum matrix elastic, plastic and void evolution properties used in LE-VCFEM simulations.

| E (GPa) | ν | γ_0 (GPa $^{-1}$ s $^{-1}$) | p | f_0 | f_c | f_f | ϵ_N | s_N | f_N |
|-----------|-------|-------------------------------------|-----|-------|-------|-------|--------------|-------|-------|
| 70 | 0.35 | 8.086 | 1 | 0.001 | 0.15 | 0.25 | 0.10 | 0.075 | 0.08 |

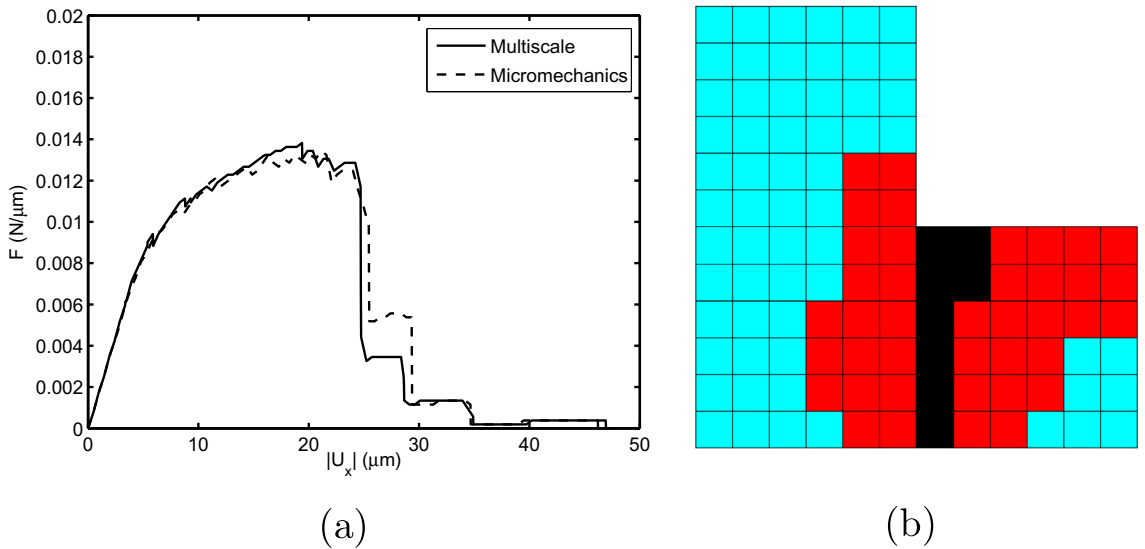


Fig. 10. (a) Comparing the total reaction force F at $x = 576 \mu\text{m}$ as a function of the applied displacement U_x by multi-level and micromechanical analyses; (b) evolved adaptive multi-level mesh at the end of simulation. (Legend: *level-0* (turquoise), *level-1* (blue), *level-2 & level-tr* (red), sealed elements (black)). (For interpretation of the references to color in this figure legend, the reader is referred to the web version of this article.)

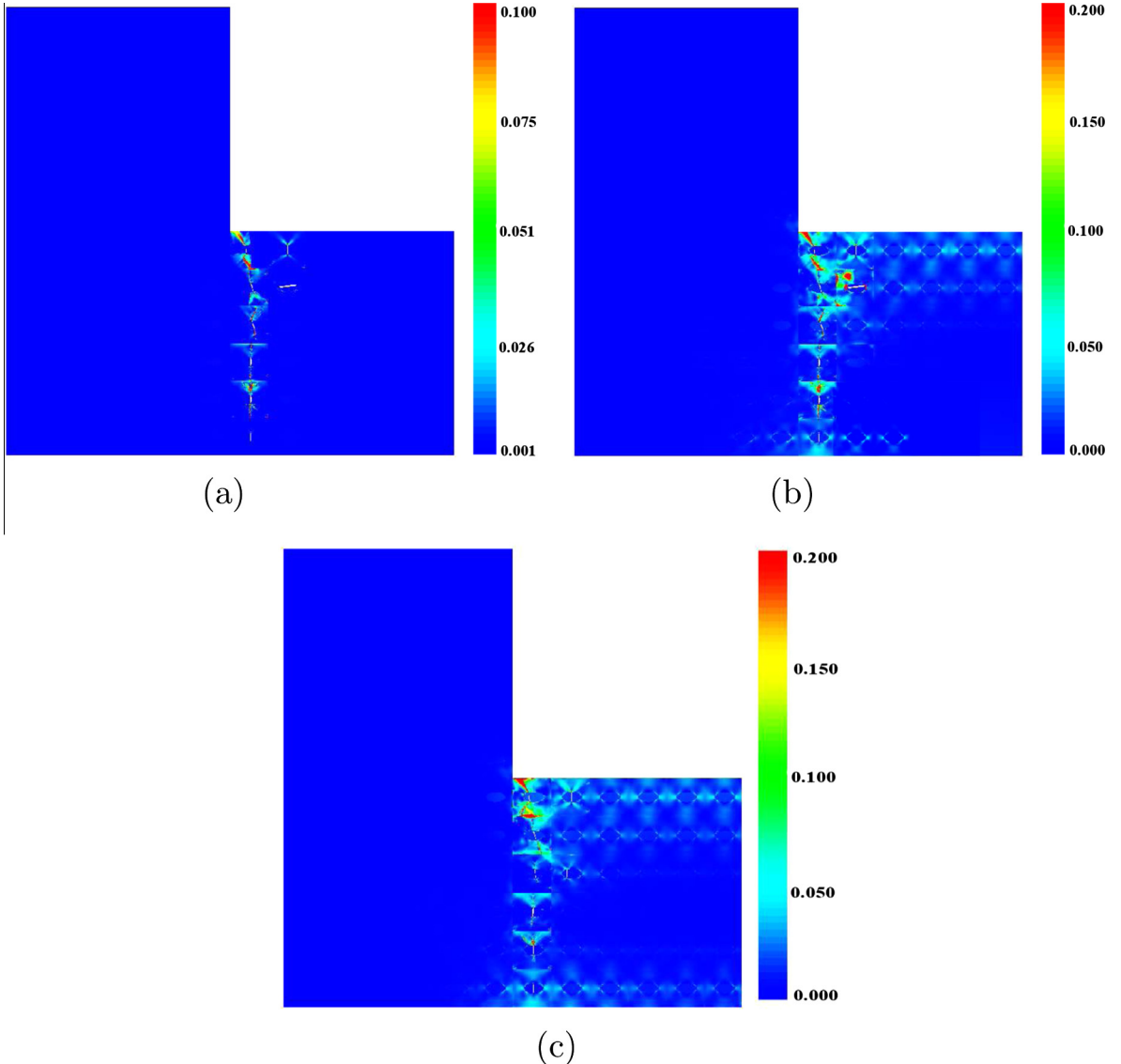


Fig. 11. Contour plots showing the final crack path at complete failure of the structure: (a) void volume fraction f and (b) equivalent plastic strain $\bar{\epsilon}_M^p$ by the multi-level model, and (c) equivalent plastic strain $\bar{\epsilon}_M^p$ by the micromechanical model.

$8 \times 32 = 256$ macro-scale elements, each of which has the dimensions $48 \mu\text{m} \times 48 \mu\text{m}$ as shown in Fig. 15. The constitutive model for this domain is the rate-dependent homogenization-based continuum plasticity-damage or HCPD model described in Section 2.1.3. The statistically equivalent representative volume element for this microstructure has been determined in Ghosh et al. (2009) to be of the size $48 \mu\text{m}$ as shown in Fig. 1(b). The HCPD model has been developed in Dondeti et al. (2012) by homogenizing results of LE-VCFEM-based micromechanical analysis, for which the inclusion and matrix material parameters are listed in Tables 1 and 2 respectively and plotted in Fig. 6.

6.1. Parameters in the HCPD model for level-0 elements

Parameters for the rate-dependent HCPD model are calibrated for the SERVE in Fig. 1(b) in Dondeti et al. (2012). The anisotropy parameters F, G, H and C in Eq. (12) and the yield strength $Y_f(W_p)$ in Eq. (13) are derived in Dondeti et al. (2012) as functions of the evolving plastic work W_p as shown in Fig. 13. The homogenized viscoplastic parameters in Eq. (14) are $\Gamma_0 = 6.13 \text{GPa}^{-1}\text{s}^{-1}$ and $P = 1$. The parameters in Eq. (11) are estimated as $Q_1 = 1.89$ and $Q_2 = 1.01$. The parameters e_0 and m in Eqs. (16) are plotted in Figs. 14 as functions of the local strain-rate. The anisotropy parameters A, B and C have functional forms of an ellipse in terms of the principal strain angle θ_p . The values

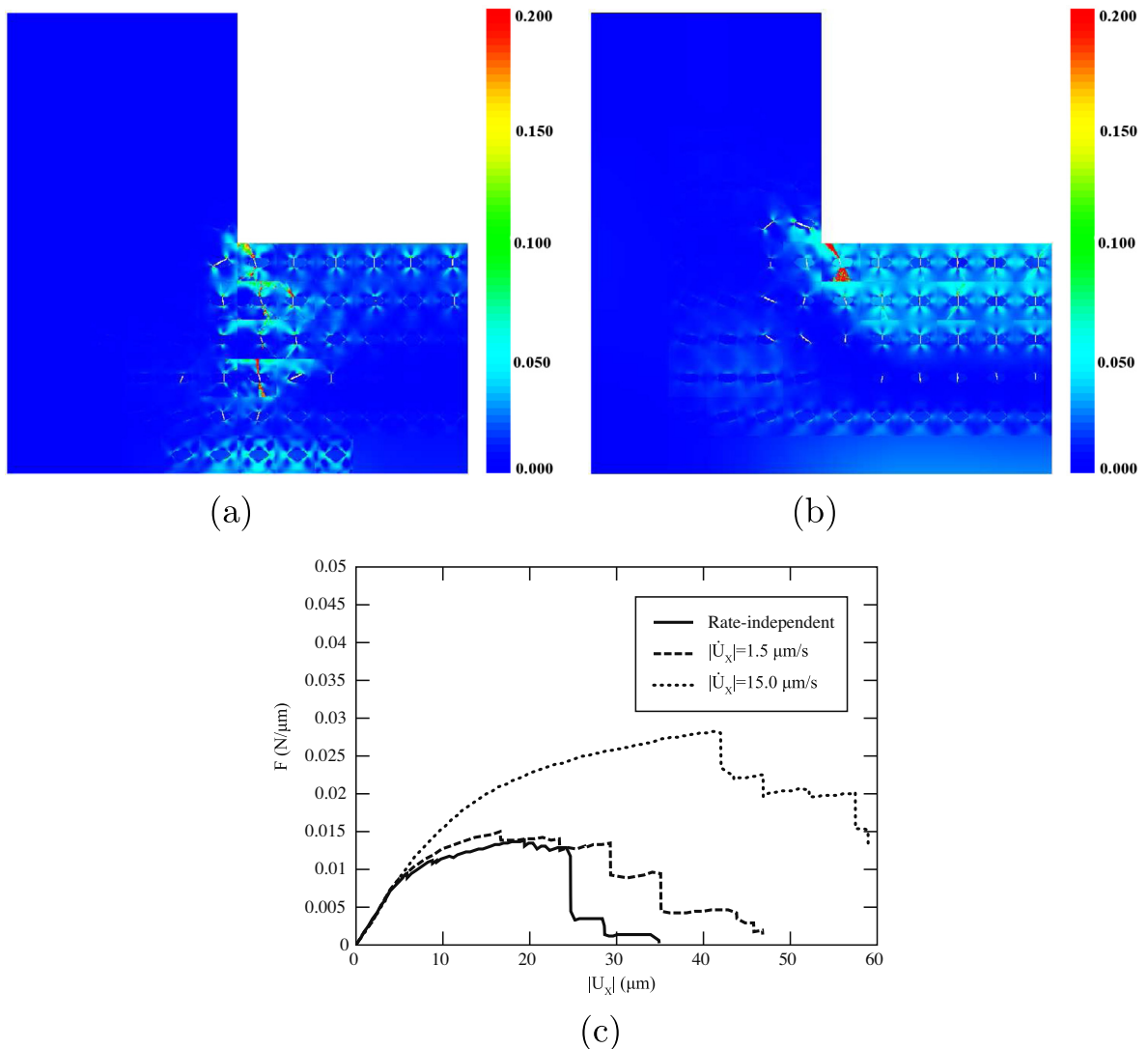


Fig. 12. Contour plots of the equivalent plastic strain $\bar{\epsilon}_M^p$ for different loading rates: (a) $\dot{U}_x = -1.5 \mu\text{m/s}$, (b) $\dot{U}_x = -15.0 \mu\text{m/s}$, and (c) reaction force F at $x = 576 \mu\text{m}$ as function of the applied displacement for two loading rates.

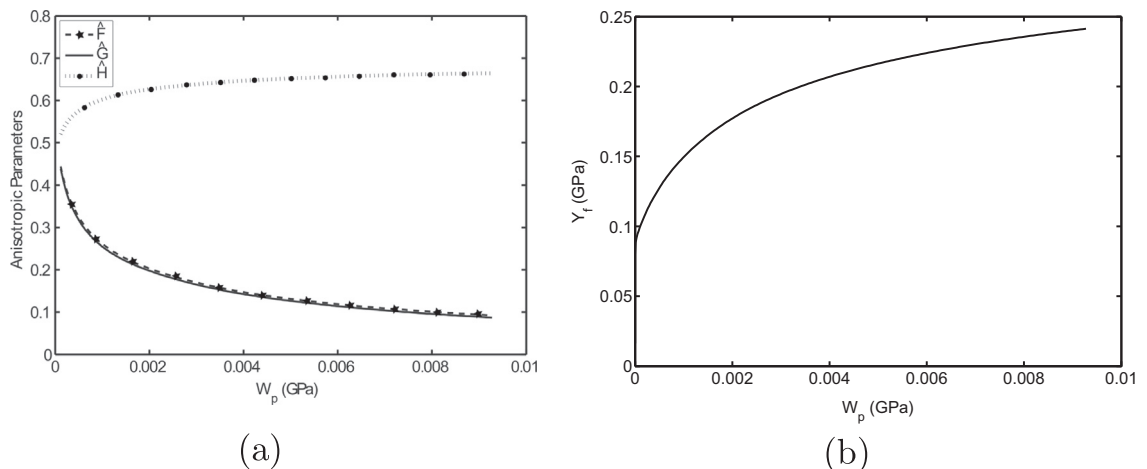


Fig. 13. (a) Evolution of anisotropy parameters \hat{F} , \hat{G} and \hat{H} , (b) yield stress in shear Y_f with plastic work for SERVE in Fig. 1(b).

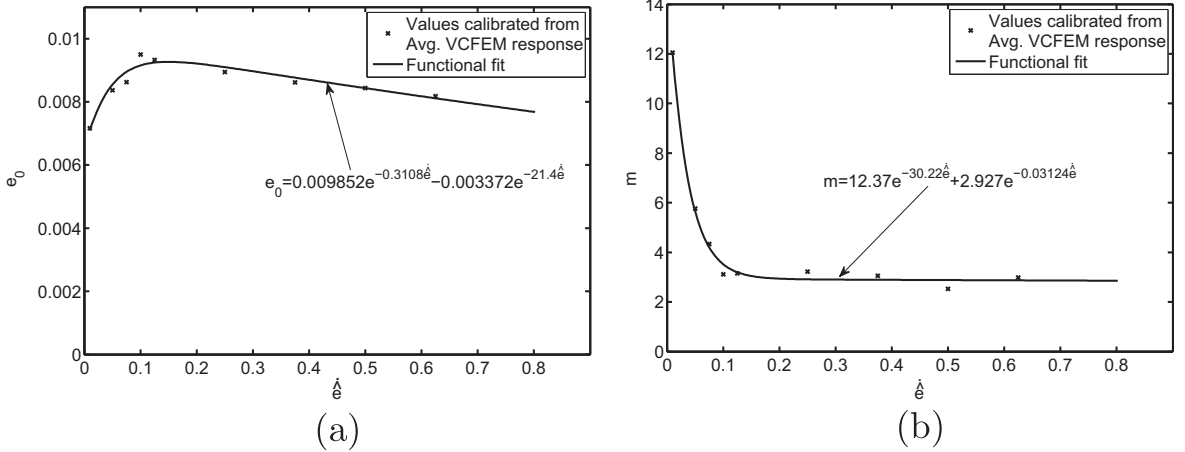


Fig. 14. Evolution of parameter (a) e_0 , and (b) m with local strain-rate $\dot{\epsilon}$.

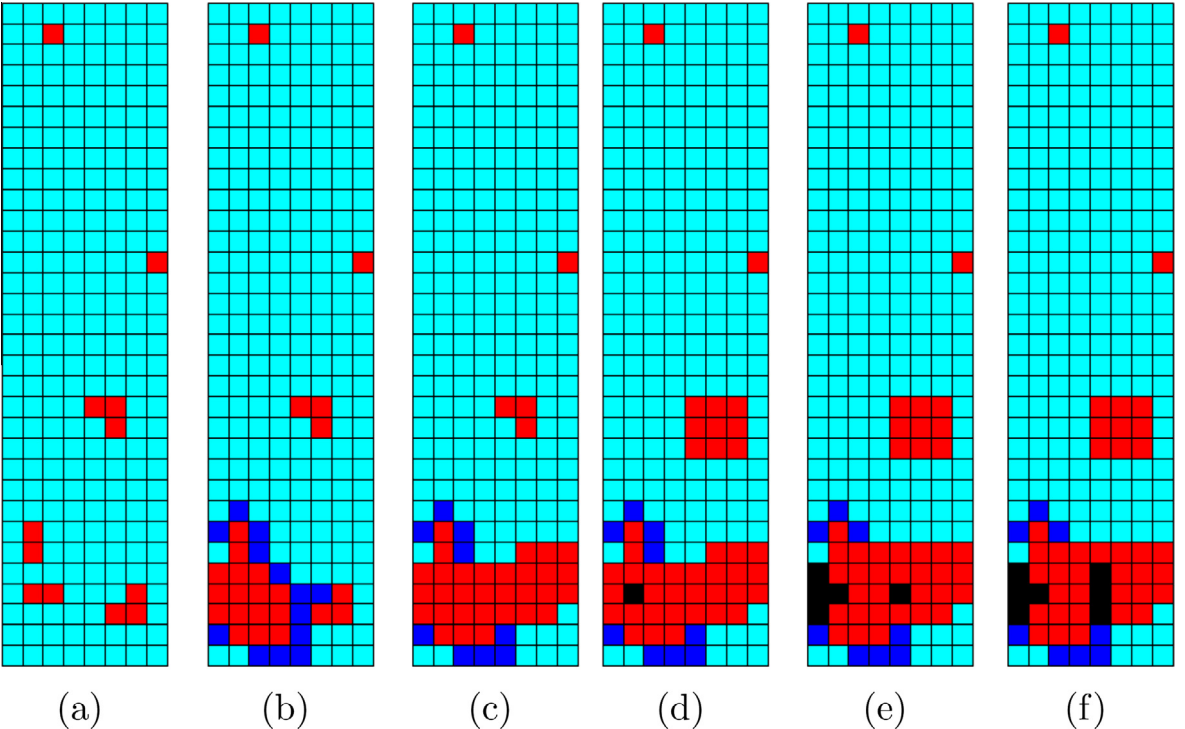


Fig. 15. Evolution of the adaptive multi-level mesh for the multi-scale analysis of a rectangular specimen loaded in tension at: (a) $U = 0$, (b) $U = 7.8 \mu\text{m}$, (c) $U = 10.3 \mu\text{m}$, (d) $U = 13.2 \mu\text{m}$, (e) $U = 13.5 \mu\text{m}$, (f) $U = 13.7 \mu\text{m}$. (Legend: level-0 (turquoise), level-1 (blue), level-2 & level-tr (red), sealed elements (black)). (For interpretation of the references to color in this figure legend, the reader is referred to the web version of this article.)

corresponding to the major and minor axes are respectively $A(\theta_p = 0^\circ) = 0.0$, $A(\theta_p = 90^\circ) = 1.01$, $B(\theta_p = 0^\circ) = 0.67$, $B(\theta_p = 90^\circ) = 0.66$, and $C(\theta_p = 0^\circ) = 0.66$, $C(\theta_p = 90^\circ) = 0.69$.

6.2. Initial model and level changes in a tension test

In the tensile test, the specimen is loaded in uniaxial tension along the vertical (y) direction by prescribing the

following boundary conditions: $U_y = \Delta U$ at $y = 1536 \mu\text{m}$, $U_y = 0$ at $y = 0$, $(U_x = 0$ at $(x, y) = (0, 0)$).

The necessity for combining multi-scale characterization with multi-scale modeling has been advocated in earlier papers by Ghosh in Ghosh et al. (2006); Ghosh et al. (2009); Ghosh et al. (2008). This is realized in this problem as well. Simulation of the tensile specimen with an initial computational domain containing only macroscopic level-0 elements leads to uniform states of stress and strain for the entire domain. Consequently, the level change criteria

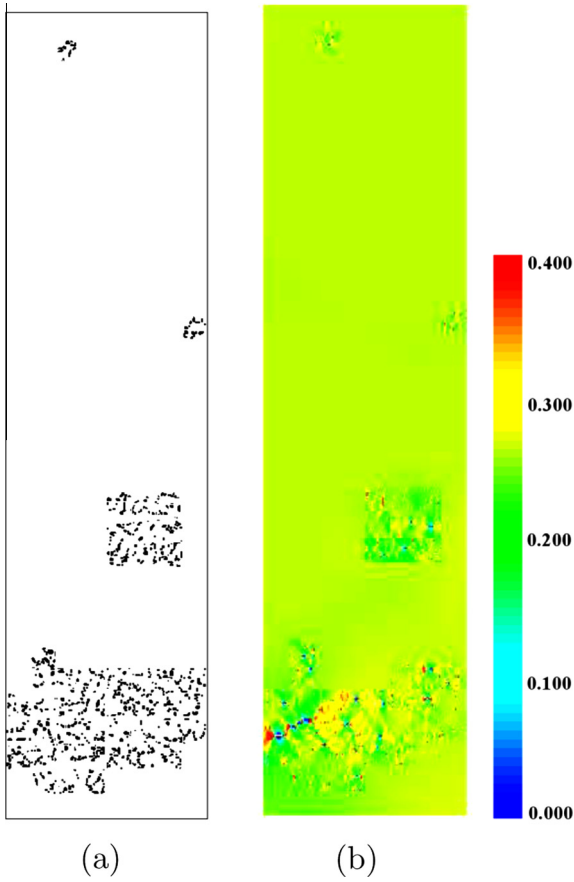


Fig. 16. (a) Underlying microstructure of the *level-2* elements in the multi-level mesh, and (b) contour plot of microscopic stress σ_{yy} (GPa) for the computational domain of the tensile specimen at an applied displacement $U_y = 13.0 \mu\text{m}$.

in Eqs. (23), (26), and (27) are not able to identify the regions at which microscopic damage first initiates, grows and coalesces. This limitation is overcome by modifying

the initial computational model using results of micro-structural characterization. In Paquet et al. (2011a,b), it has been established that regions characterized by high values of local inclusion volume fraction and clustering have critically low ductility. A parameter \tilde{f} , defined in terms of the inclusion volume fraction V_f and cluster contour index ι as:

$$\tilde{f} = \frac{\iota}{0.929 - 1.83V_f} \quad (42)$$

has been shown in Paquet et al. (2011a) to be a very good indicator of local ductility in a microstructure. This parameter is used to seek out the critical regions in the computational domain Ω_{l0} where ductile fracture is likely to initiate in the microstructure. Prior to the multi-scale analysis, \tilde{f} is computed for the local microstructure of each of the 256 *level-0* elements. Six critical elements (regions) are identified as "hot-spots" for premature nucleation of ductile cracks. Correspondingly, in a concurrent setting, these are modeled as *level-2* elements from the start. The remainder of all elements in the initial multi-level mesh are *level-0* as shown in Fig. 15(a). Adaptive level change is now activated based on the criteria in Eqs. (23), (26), and (27). The constants used in the criteria are $C_2 = 0.2$, $C_3 = 0.1$, and $C_4 = 0.1$. Mesh adaptivity with *h*-adaptation algorithm is not considered in this example.

6.3. Simulation through complete micro-cracking

With increasing deformation, non-uniformities arise in the microscopic sub-domains Ω_{l2} due to cracking of silicon inclusions and plastic deformation of the aluminum matrix, thus altering the initial homogeneity of the macro-scale stress and strain fields. This leads to high gradients in the void volume fraction \tilde{f} that switch the surrounding *level-0* elements to *level-1* elements, and subsequently precipitates *level-2* elements in these regions. This adaptive transition of macroscopic to microscopic elements, shown in Fig. 15, continues with the evolution of damage primarily in a direction perpendicular to the applied load. These

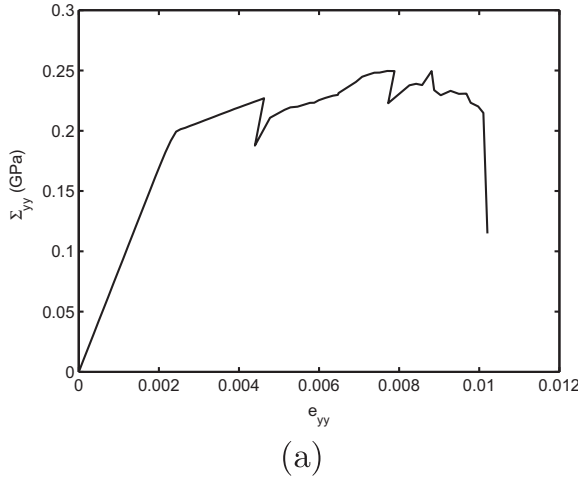
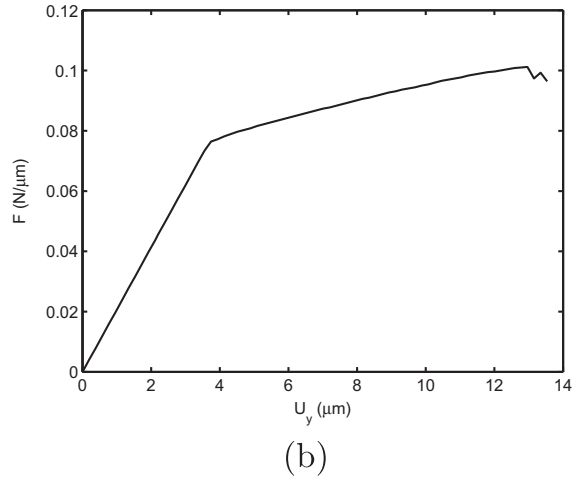


Fig. 17. (a) Local averaged stress-strain response of the first *level-2* element sealed during multi-scale simulation, and (b) overall response of the tensile specimen obtained with the multi-scale model. The total reaction force F at $y = 1536 \mu\text{m}$ is plotted as function of the applied displacement U_y .



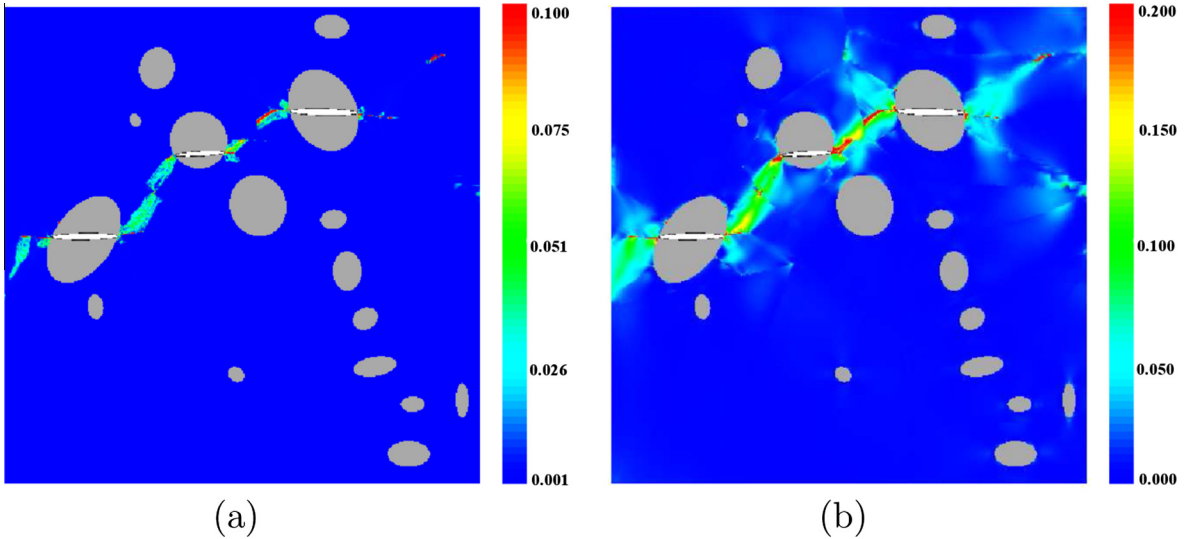


Fig. 18. Contour plots showing the final crack path at complete failure of the first *level-2* element during the multi-scale simulation: (a) void volume fraction f , and (b) equivalent plastic strain ϵ_M^p .

microscopic elements in Ω_{l2} coalesce with the evolving ductile deformation and damage as shown in Fig. 15(f) for an applied displacement of $U_y = 10.3 \mu\text{m}$. Subsequently, the evolution of microscopic sub-domains stabilizes until localization of damage within a *level-2* microstructure leads to its complete failure. The first complete *level-2* element failure and consequent sealing occurs at an applied displacement $U_y = 13.2 \mu\text{m}$. Sealing of a *level-2* element due to complete failure of its microstructure is activated when a sharp drop in the homogenized stress-strain response of the element is detected. The contour plot of the microscopic stress component σ_{yy} at the onset of local failure of the *level-2* element is given in Fig. 16(b). The figure shows localization of stresses due to local ductile failure. An image of the underlying microstructure for the Ω_{l2} sub-domain is given in Fig. 16(a).

The abrupt drop in the averaged stress response of a *level-2* element is associated with the unstable growth of damage in the microstructure. The homogenized stress-strain response of the first sealed element is plotted in Fig. 17(a). The local softening of the element causes a drop in the force-displacement response of the tensile specimen as seen in the Fig. 17(b). Contour plots of microscopic void volume fraction and equivalent plastic strain for the newly sealed element are also shown in Fig. 18. These plots clearly demonstrate that a dominant ductile crack has propagated through the *level-2* microstructure. After the first element sealing has occurred, an increase in local stresses and strains in the remaining *level-2* elements results in an acceleration of damage growth. This leads to the propagation of sealed elements as seen in the Figs. 15(d)–(f). It is also observed in Fig. 15(j) that a second macro-crack emerges from the microstructure. This failure process continues until the macro-cracks become extremely unstable and the final failure of the structure occurs. The force-displacement response in tension of the specimen shows a very low ductility after the maximum tensile

stress has been reached. The multi-scale simulation leads to tensile plots having the same characteristics as those obtained from experiments for the aluminum alloy W319 in Hu and Ghosh (2008) and the aluminum alloy AS7GU in Chisaka (2009).

This numerical example clearly demonstrates the effectiveness of the multi-level model in capturing multi-scale ductile fracture mechanisms in cast aluminum alloys, consisting of damage nucleation by inclusion cracking, followed by void nucleation, growth, and coalescence in the matrix. It averts the need for introducing artificial non-uniformities such as local variations of void volume fraction, or geometric discontinuities such as notch, for capturing damage localization in the microstructural domain. Localization of damage naturally arises due to heterogeneities in the microstructure morphology.

7. Summary and conclusions

This paper assimilates a variety of complementary ingredients to create a novel two-way multi-level modeling framework that is necessary for modeling ductile fracture in heterogeneous aluminum alloys. A unique feature is the incorporation of detailed microstructural information acquired from micrographs. The two-way multi-level model involves both bottom-up and top-down structure-material coupling. Bottom-up coupling invokes hierarchical multi-scaling and implements homogenization to yield reduced-order constitutive relations for efficient computations at the higher scales. Top-down coupling is facilitated in a concurrent way, such that detailed lower scale (micro-mechanical in this case) models can be directly embedded in the higher-scale models at regions of evolving intense localization and damage. This facility successfully captures micromechanisms of ductile fracture in a deforming material. The adaptive capability enables this top-down

coupling for the evolutionary problems in an automatic fashion, without user intervention.

Micromechanical analysis in microscopic levels of this framework is performed by the locally enhanced Voronoi cell FEM or LE-VCFEM for ductile fracture in heterogeneous materials, previously developed by the authors in Paquet et al. (2011a,b). Ductile fracture mechanisms consisting of brittle inclusion cracking, followed by void initiation, growth and coalescence in the matrix are readily modeled with LE-VCFEM. The multi-level framework includes efficient macroscopic level analysis in regions where homogenization is valid. The homogenization based continuum plasticity-damage (HCPD) model, used for the macroscopic analysis in these regions, is derived by homogenizing evolving variables in the microstructural RVE when subjected to various loading conditions. An intermediate level is included in the model for identifying regions, where homogenization ceases to hold. Subsequently, the region is switched to that where detailed micromechanical computations are performed. This local enrichment allows the multi-scale model to capture the evolution of damage. The microscopic sub-regions propagate following the path of microstructural damage from initiation to final fracture.

The multi-level model is validated against pure micromechanical simulations for accuracy. Numerical simulations conclude that ductile fracture is sensitive to the applied loading rate, with higher velocities lead to more diffused damage in the structure. The multi-level model is also implemented to solve a multi-scale ductile fracture problem involving microstructures of cast aluminum alloys. Ductile fracture is very sensitive to the actual microstructural morphology. It is shown that damage initiation and growth can be effectively captured by the model without the introduction of any artificial discontinuity or defect. Multi-scale characterization of the actual microstructure is used to identify critical regions, at local micromechanical analyses are concurrently conducted.

The multi-scale model developed in this paper is quite unique and different from many models proposed in the literature in that it does not make any simplifying assumptions on the overall response of microstructural domains in which localization and failure occur. Few models represent the concurrent setting to manifest localization of deformation and damage within the microstructure. The multi-level model along with the adaptive capabilities developed in this paper impart the necessary efficiency that is essential to conduct such large scale computations.

Acknowledgments

This work has been supported by the National Science Foundation NSF Div Civil and Mechanical Systems Division through the GOALI Grant No. CMS-0308666 (Program Director: Dr. M. Dunn), by the Department of Energy Aluminum Visions program through Grant No. A5997. This sponsorship is gratefully acknowledged. The authors are grateful to Drs. Xuming Su, and James Boileau of Ford Research Laboratory for invaluable discussions and for micrographs and samples used. Computer support by the Ohio Supercomputer Center through Grant PAS813-2 is also gratefully acknowledged.

References

- Caceres, C., Griffiths, J., 1996. Damage by the cracking of silicon particles in an Al-7Si-0.4Mg casting alloy. *Acta Mater.* 44, 25–33.
- Caceres, C., 1999. Particle cracking and the tensile ductility of a model Al-Si-Mg composite system. *Aluminum Trans.* 1, 1–13.
- Wang, Q., Caceres, C., Griffiths, J., 2003. Damage by eutectic particle cracking in aluminum casting alloys A356/357. *Metall. Mater. Trans. A* 34, 2901–2912.
- Steglich, D., Brocks, W., 1997. Micromechanical modeling of the behavior of ductile materials including particles. *Comput. Mater. Sci.* 9, 7–17.
- Lim, L., Dunne, F., 1996. Modeling void nucleation and growth processes in a particle-reinforced metal matrix composite material. *Comput. Mater. Sci.* 5, 177–186.
- Negre, P., Steglich, D., Brocks, W., Kocak, M., 2003. Numerical simulation of crack extension in aluminium welds. *Comput. Mater. Sci.* 28, 723–731.
- Huber, G., Brechet, Y., Pardoen, T., 2005. Predictive model for void nucleation and void growth controlled ductility in quasi-eutectic cast aluminium alloys. *Acta Mater.* 53, 2739–2749.
- Llorca, J., Gonzalez, C., 1998. Microstructural factors controlling the strength and ductility of particle-reinforced metal-matrix composites. *J. Mech. Phys. Solids* 46, 1–28.
- Llorca, J., Segurado, J., 2004. Three-dimensional multiparticle cell simulations of deformation and damage in sphere-reinforced composites. *Mater. Sci. Eng. A* 365, 267–274.
- Moorthy, S., Ghosh, S., 1998. A Voronoi cell finite element model for particle cracking in elastic-plastic composite materials. *Comput. Meth. Appl. Mech. Eng.* 151, 377–400.
- Ghosh, S., Moorthy, S., 1998. Particle fracture simulation in non-uniform microstructures of metal–matrix composites. *Acta Mater.* 46, 965–982.
- Hu, C., Ghosh, S., 2008. Locally enhanced Voronoi cell finite element model (LE-VCFEM) for simulating evolving fracture in ductile microstructures containing inclusions. *Int. J. Numer. Meth. Eng.* 76, 1955–1992.
- Paquet, D., Ghosh, S., 2011a. Microstructural effects on ductile fracture in heterogeneous materials. Part I: Sensitivity analysis with LE-VCFEM. *Eng. Fract. Mech.* 78, 205–225.
- Paquet, D., Ghosh, S., 2011b. Microstructural effects on ductile fracture in heterogeneous materials. Part II: Application to cast aluminum microstructures. *Eng. Fract. Mech.* 78, 226–233.
- Moorthy, S., Ghosh, S., 2000. Adaptivity and convergence in the Voronoi cell finite element model for analyzing heterogeneous materials. *Comput. Methods Appl. Mech. Eng.* 185, 37–74.
- Ghosh, S., 2011. Micromechanical Analysis and Multi-scale Modeling Using the Voronoi Cell Finite Element Method. CRC Press, Taylor & Francis, Boca Raton, FL.
- Ghosh, S., Ling, Y., Majumdar, B., Kim, R., 2000. Interfacial debonding analysis in multiple fiber reinforced composites. *Mech. Mater.* 32, 561–591.
- Guedes, J.M., Kikuchi, N., 1990. Preprocessing and postprocessing for materials based on the homogenization method with adaptive finite element methods. *Comput. Methods Appl. Mech. Eng.* 83, 143–198.
- Ghosh, S., Lee, K., Moorthy, S., 1995. Multiple scale analysis of heterogeneous elastic structures using homogenization theory and Voronoi cell finite element method. *Int. J. Solids Struct.* 32, 27–62.
- Feyel, F., Chaboche, J.-L., 2000. FE² multiscale approach for modelling the elasto-viscoplastic behaviour of long fibre SiC/Ti composite materials. *Comput. Methods Appl. Mech. Eng.* 183, 309–330.
- Terada, K., Kikuchi, N., 2001. A class of general algorithms for multi-scale analyses of heterogeneous media. *Comput. Methods Appl. Mech. Eng.* 190, 5427–5464.
- Miehe, C., Koch, A., 2002. Computational micro-to-macro transitions of discretized microstructures undergoing small strains. *Arch. Appl. Mech.* 72, 300–317.
- Ghosh, S., Lee, K., Moorthy, S., 1996. Two scale analysis of heterogeneous elastic-plastic materials with asymptotic homogenization and Voronoi cell finite element model. *Comput. Methods Appl. Mech. Eng.* 132, 63–116.
- Lee, K., Ghosh, S., 1996. Small deformation multi-scale analysis of heterogeneous materials with the Voronoi cell finite element model and homogenization theory. *Comput. Mater. Sci.* 7, 131–146.
- Moulinec, H., Suquet, P., 2001. A computational scheme for linear and nonlinear composites with arbitrary phase contrasts. *Int. J. Numer. Methods Eng.* 52, 139–160.
- Zohdi, T., Oden, J., Rodin, G., 1999. Hierarchical modeling of heterogeneous solids. *Comp. Meth. Appl. Mech. Eng.* 172, 3–25.

- Oden, J., Zohdi, T., 1997. Analysis and adaptive modeling of highly heterogeneous elastic structures. *Comp. Meth. Appl. Mech. Eng.* 148, 367–391.
- Benssousan, A., Lions, J.L., Papanicoulou, G., 1978. *Asymptotic Analysis for Periodic Structures*. North Holland, Amsterdam.
- Sanchez-Palencia, E., 1983. Homogenization method for the study of composite media. In: Verhulst, F. (Ed.), *Asymptotic Analysis II*, Lecture Notes in Mathematics, vol. 985. Springer Berlin, Heidelberg, pp. 192–214.
- Kouznetsova, V.G., Geers, M.G.D., Brekelmans, W.A.M., 2004. Multi-scale second-order computational homogenization of multi-phase materials: a nested finite element solution strategy. *Comput. Methods Appl. Mech. Eng.* 193, 5525–5550.
- Luscher, D.J., McDowell, D.L., Bronkhorst, C.A., 2010. A second gradient theoretical framework for hierarchical multiscale modeling of materials. *Int. J. Plast.* 26, 1248–1275.
- Verner, F.J., Liu, W.K., Olson, G., 2008. A micromorphic model for the multiple scale failure of heterogeneous materials. *J. Mech. Phys. Solids* 56, 1320–1347.
- Fish, J., Kuznetsov, S., 2010. Computational continua. *Int. J. Numer. Methods Eng.* 84, 774–802.
- Loehnert, S., Belytschko, T., 2007. A multiscale projection method for macro/microcrack simulations. *Int. J. Numer. Methods Eng.* 71, 1466–1482.
- Massart, T.J., Peerlings, R.H.J., Geers, M.G.D., 2007. An enhanced multi-scale approach for masonry wall computations with localization of damage. *Int. J. Numer. Methods Eng.* 69, 1022–1059.
- Belytschko, T., Loehnert, S., Song, J.-H., 2008. Multiscale aggregating discontinuities: a method for circumventing loss of material stability. *Int. J. Numer. Methods Eng.* 73, 869–894.
- Song, J.-H., Belytschko, T., 2009. Multiscale aggregating discontinuities method for micro-macro failure of composites. *Composites: Part B* 40, 417–426.
- Vemaganti, K.S., Oden, J.T., 2001. Estimation of local modeling error and goal-oriented adaptive modeling of heterogeneous materials (part II): a computational environment for adaptive modeling of heterogeneous elastic solids. *Comput. Methods Appl. Mech. Eng.* 190, 6089–6124.
- Markovic, D., Ibrahimbegovic, A., 2004. On micro-macro interface conditions for micro scale based FEM for inelastic behavior of heterogeneous materials. *Comput. Methods Appl. Mech. Eng.* 193, 5503–5523.
- Temizer, I., Wriggers, P., 2011. An adaptive multiscale resolution strategy for the finite deformation analysis of microheterogeneous structures. *Comput. Methods Appl. Mech. Eng.* 200, 2639–2661.
- Kim, D.-J., Pereira, J.P., Duarte, C.A., 2010. Analysis of three-dimensional fracture mechanics problems: a two-scale approach using coarse-generalized FEM meshes. *Int. J. Numer. Methods Eng.* 81, 335–365.
- Miehe, C., Bayreuther, C.G., 2007. On multiscale FE analyses of heterogeneous structures: from homogenization to multigrid solvers. *Int. J. Numer. Methods Eng.* 71, 1135–1180.
- Fish, J., Shek, K., 2000. Multiscale analysis of composite materials and structures. *Compos. Sci. Technol.* 60, 2547–2556.
- Zohdi, T., Wriggers, P., 1999. A domain decomposition method for bodies with heterogeneous microstructure based on material regularization. *Int. J. Sol. Struct.* 36, 2507–2525.
- Raghavan, P., Moorthy, S., Ghosh, S., Pagano, N.J., 2001. Revisiting the composite laminate problem with an adaptive multi-level computational model. *Compos. Sci. Technol.* 61, 1017–1040.
- Raghavan, P., Ghosh, S., 2004. Adaptive multi-scale computational modeling of composite materials. *Comp. Model. Eng. Sci.* 5, 151–170.
- Raghavan, P., Ghosh, S., 2004. Concurrent multi-scale analysis of elastic composites by a multi-level computational model. *Comput. Methods Appl. Mech. Eng.* 193, 497–538.
- Lee, K., Moorthy, S., Ghosh, S., 1999. Multiple scale computational model for damage in composite materials. *Comput. Methods Appl. Mech. Eng.* 172, 175–201.
- Raghavan, P., Li, S., Ghosh, S., 2004. Two scale response and damage modeling of composite materials. *Finite Elem. Anal. Des.* 40, 1619–1640.
- Ghosh, S., Bai, J., Raghavan, P., 2007. Concurrent multi-level model for damage evolution in microstructurally debonding composites. *Mech. Mater.* 39, 241–266.
- Valiveti, D.M., Ghosh, S., 2007. Domain partitioning of multi-phase materials based on multi-scale characterizations: a preprocessor for multi-scale modeling. *Int. J. Numer. Meth. Eng.* 69 (8), 1717–1754.
- Ghosh, S., Valiveti, D., Harris, S., Boileau, J., 2006. A domain partitioning based pre-processor for multi-scale modeling of cast aluminum alloys. *Model. Simul. Mater. Sci. Eng.* 14, 1363–1396.
- Ghosh, S., Bai, J., Paquet, D., 2009. Homogenization-based continuum plasticity-damage model for ductile failure of materials containing heterogeneities. *J. Mech. Phys. Sol.* 57, 1017–1044.
- Paquet, D., Dondeti, P., Ghosh, S., 2011. Dual-stage nested homogenization for rate-dependent anisotropic elasto-plasticity model of dendritic cast aluminum alloys. *Int. J. Plast.* 27, 1677–1701.
- Dondeti, P., Paquet, D., Ghosh, S., 2012. A rate-dependent homogenization based continuum plasticity-damage (HCPD) model for dendritic cast aluminum alloys. *Eng. Fract. Mech.* 89, 75–97.
- Gurson, A.L., 1977. Continuum theory of ductile rupture by void nucleation and growth: Part I. Yield criteria and flow rule for porous ductile media. *J. Eng. Mater. Technol.* 99, 2–15.
- Chu, C.C., Needleman, A., 1980. Void nucleation effects in biaxially stretched sheets. *J. Eng. Mater. Technol.* 102, 249–256.
- Tvergaard, V., 1982. On localization in ductile materials containing voids. *Int. J. Fract.* 18, 237–251.
- Tvergaard, V., Needleman, A., 1984. Analysis of the cup-cone fracture in a round tensile bar. *Acta Metall.* 32, 157–169.
- Perzyna, P., 1966. Fundamental problems in viscoplasticity. *Adv. Appl. Mech.* 9, 243–377.
- Hill, R., 1948. A theory of the yielding and plastic flow of anisotropic metals. *Proc. R. Soc. A: Math. Phys.* 193, 281–297.
- Hill, R., 1972. On constitutive macro-variables for heterogeneous solids at finite strain. *Proc. R. Soc. A: Math. Phys.* 326, 131–147.
- Bass, J.M., Oden, J.T., 1987. Adaptive finite element methods for a class of evolution problems in viscoplasticity. *Int. J. Eng. Sci.* 6, 623–653.
- Zienkiewicz, O., Zhu, J., 1992. The superconvergent patch recovery and a posteriori error estimates. Part 1: The recovery technique. *Int. J. Numer. Methods Eng.* 33, 1331–1364.
- Ghosh, S., Valiveti, D., Hu, C., Bai, J., 2009. A multi-scale framework for characterization and modeling ductile fracture in heterogeneous aluminum alloys. *Int. J. Multiscale Model. Comp.* 1, 21–55.
- Ghosh, S., Valiveti, D., Hu, C., Bai, J., 2008. Multi-scale characterization and modeling of ductile failure in cast aluminum alloys. *Int. J. Comp. Meth. Eng. Sci.* 9, 25–42.
- Chisaka, K., 2009. Microstructure characterization and mechanical properties of cast aluminum alloy AS7GU, advisor: S. Ghosh, B.S. Thesis. The Ohio State University (December).